

# A micromorphic model for the multiple scale failure of heterogeneous materials

Franck J. Vernerey<sup>a,d,\*</sup>, Wing Kam Liu<sup>b,\*\*</sup>, Brian Moran<sup>b</sup>, Gregory Olson<sup>c</sup>

<sup>a</sup>*Department of Civil and Environmental Engineering, Northwestern University, 2145 Sheridan Road, Evanston, IL 60208-3111, USA*

<sup>b</sup>*Department of Mechanical Engineering, Northwestern University, 2145 Sheridan Road, Evanston, IL 60208-3111, USA*

<sup>c</sup>*Department of Material Science and Engineering, Northwestern University, 2145 Sheridan Road, Evanston, IL 60208-3111, USA*

<sup>d</sup>*Department of Civil, Environmental and architectural Engineering, University of Colorado at Boulder, 1111 engineering Drive, 428 UCB, ECOT 422, Boulder, CO 80309-0428, USA*

Received 1 December 2006; received in revised form 20 June 2007; accepted 13 September 2007

---

## Abstract

The multi-scale micromorphic theory developed in our previous paper [Vernerey, F.J., Liu, W.K., Moran, B., 2007. Multi-scale micromorphic theory for hierarchical materials. *J. Mech. Phys. Solids*, doi:10.1016/j.jmps.2007.04.008] is used to predict the failure of heterogeneous materials illustrated by a high strength steel alloy possessing two populations of hard particles distributed at two distinct length scales in an alloy matrix. To account for the effect and size of microstructural features during fracture, additional kinematic variables are added, giving rise to the couple stresses associated with each population of particles. The various stress and strain measures must satisfy a set of coupled multi-scale governing equations derived from the principle of virtual power. A three-scale constitutive model is then developed to represent the failure of the alloy from nucleation, growth and coalescence of voids from each population of particles. For this, three distinct yield functions, each corresponding to a different scale, are introduced. Cell model simulations using finite elements are performed to determine the constitutive relations based on the key microstructural features. Two-dimensional failure analyses are then presented in tension and in shear, and show good agreement with direct numerical simulation of the microstructure.

© 2007 Published by Elsevier Ltd.

*Keywords:* Multi-scale micromorphic theory; Homogenization; Finite elements; Constitutive relations; Materials stability

---

## 1. Introduction

Macroscopic properties are a key factor in the choice of material for a specific engineering application. Nevertheless, the origins of a material's behavior reside in the properties and their interactions that take place at the scale of its microstructure. More specifically, materials fracture strongly depends on the size, geometry, distribution and various properties of microscopic heterogeneities that can be found

---

\*Corresponding author. Tel.: +1 847 467 2401.

\*\*Corresponding author.

*E-mail addresses:* [f-vernerey@northwestern.edu](mailto:f-vernerey@northwestern.edu) (F.J. Vernerey), [w-liu@northwestern.edu](mailto:w-liu@northwestern.edu) (W.K. Liu).

in the form of grains, fibers or different size particles. In this work, we propose to use the multi-scale micromorphic theory (Vernerey et al., 2007) to study the failure of a class of heterogeneous materials that possess a hierarchical microstructure by considering the particular case of a well-studied engineering material: high strength steel.

Many pure polycrystalline metals can be considered very ductile but are generally not strong enough for most engineering applications. A way to improve strength is to add specific reinforcements in the form of particles. In the case of high strength steel, there are typically two populations of particles distributed at different length scales, commonly termed the primary and secondary particles. Secondary particles (such as titanium carbide), ranging from tens to hundreds of nanometers in size, have the effect of refining grain size during thermal processing, and hence, increase the material's strength. Primary particles (such as titanium nitride) are byproducts of manufacturing process and are generally too large (approximately 1  $\mu\text{m}$  in size) to increase the material's strength.

Ductile fracture of high strength steel is known to be controlled by the nucleation, growth and coalescence of voids around both populations of inclusions. Within the past decades, substantial efforts have been devoted to the development of continuum models based on the nucleation, growth, and coalescence from populations of inclusions. One of the best-known micromechanical models was derived by Gurson (1977); he studied the loss of load carrying capacity of a voided material during plastic deformation. In Gurson (1977), a yield criterion is derived based on the evolution of a damage parameter, the void volume fraction. Similarly, Rice and Tracey (1969) derived a model for the evolution of a void in an infinite plastic matrix. A semi-empirical relationship was developed between void straining and remote stresses in the matrix. Numerous extensions of the Gurson model have been presented in the literature. Based on numerical simulations, Needleman and Tvergaard (1984) modified the material constants of the Gurson model to provide a better description of neighboring void interactions. The interaction of voids with particles, and especially the stage of void nucleation from particles were investigated by Saje et al. (1982) and Goods and Brown (1979). Other models include a more detailed description of the void growth mechanisms. For instance, Gologanu et al. (1995) investigated the effect of void shape by considering an internal variable characterizing the eccentricity of elliptic voids. This model was later extended by Pardoen and Hutchinson (2000) to provide a more accurate description of void coalescence.

One of the major drawbacks of the above models together with all other local softening plasticity models is that they are unable to capture the size of the localization region after the onset of softening (Bazant and Jirasek, 2002). To overcome this issue, nonlocal models with the introduction of a parameter that characterizes the typical length scale of the microstructure were developed (Pijaudier-Cabot and Bazant, 1987). In this context, Leblond et al. (1994) and Tvergaard and Needleman (1995, 1997) proposed a Gurson-type model that was modified by introducing a nonlocal evolution for porosity. This method provides a convenient way of introducing a length scale in the formulation but has two main limitations: first, it is not based on the underlying failure mechanisms and second, only the scale of primary particles is accounted for. In fact, fracture of high strength steels is a complex process that involves localizations of the deformation across several length scales, given by primary and secondary particles. This paper proposes to utilize the multi-scale micromorphic theory (Vernerey et al., 2007) to incorporate deformation and length scales associated with both populations of particles. The resulting multi-scale model of high strength steel possesses several characteristics. First, it accounts for material deformation and damage across three scales, namely, the macro, or specimen scale, micro or primary particle scale, and submicro, or secondary particle scale. Second, the constitutive relation is derived from mechanism based averaging operations. Third, it remains a continuum model and therefore remains computationally affordable.

The organization of this paper is as follows. After briefly reviewing the fracture mechanisms of high strength steel, we propose a multi-scale decomposition of the material's microstructure. This gives rise to a set of equations governing the physics of material failure at each scale of interest. The constitutive relation is then introduced in the form of a multi-potential plasticity model and a nested homogenization procedure is employed at each scale of analysis. In this procedure, the micro and submicro-scale physics are related to the macroscopic stress–strain law. Finally, the model is evaluated through a one-dimensional and a two-dimensional numerical analysis of the failure of a specimen under both tensile and shear loading.

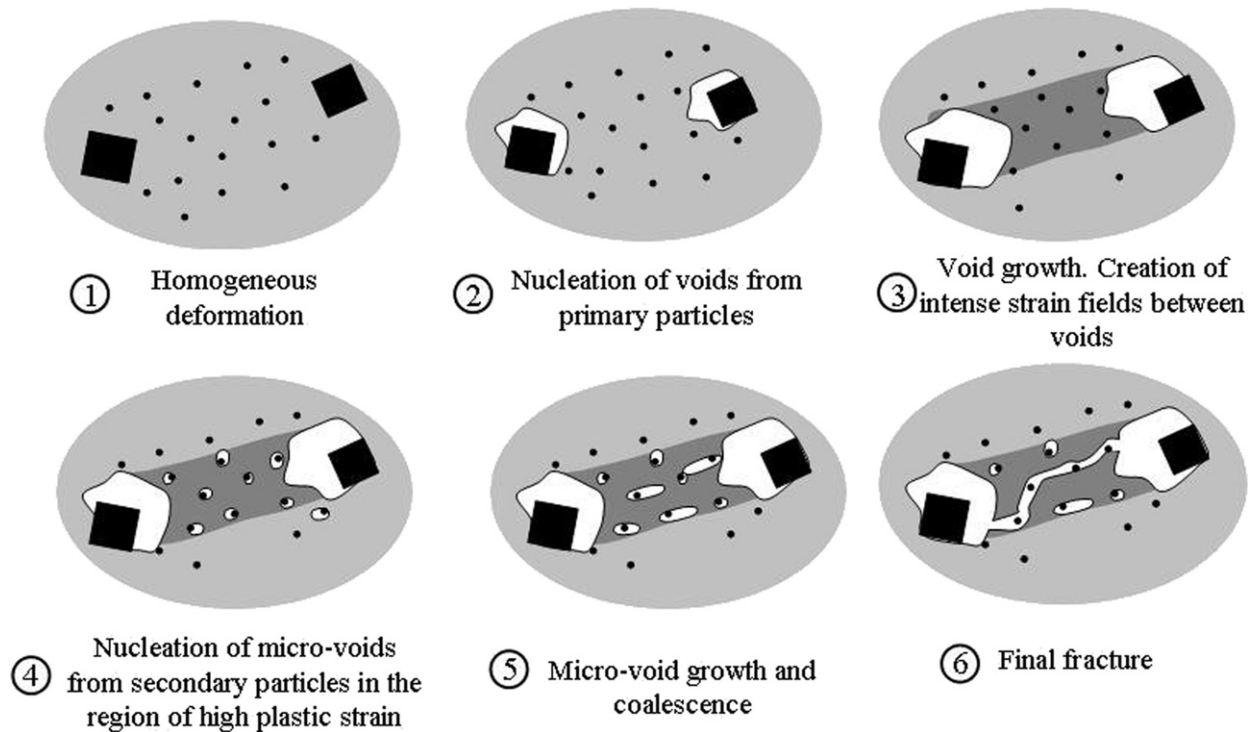


Fig. 1. Stages of ductile fracture of high strength steels.

## 2. Multi-scale model

### 2.1. Ductile fracture mechanisms

In the study of ductile fracture mechanisms, the distinct role of primary and secondary particles can be deduced by observation of the fracture surface. Because bonding at the particle–matrix interface is stronger for secondary than for primary particles, nucleation and growth of voids from primary particles occurs first. Once the voids reach a certain size, the large local plastic strains promote nucleation of microvoids at the sites of secondary particles that grow in a so-called “void sheet” linking larger voids. Finally, final failure of the material occurs when microvoids coalesce. The mechanisms of ductile fracture are summarized in Fig. 1, showing six characteristic stages.

The first subfigure gives a simplistic representation of the structure of high strength steel, with primary particles, depicted as large, square shaped inclusions and secondary particles represented by the smaller, circular inclusions. Stages 2 and 3 show the nucleation and growth of voids around primary particles. When neighboring voids interact, an inhomogeneous band of plastic deformation can be observed between cavities. As large voids grow, the intensity of plastic strain increases in these bands, eventually triggering nucleation of voids from secondary particles as shown in stage 4. Finally, stages 5 and 6, depict growth and coalescence of voids that have nucleated from secondary particles in the shear band between primary particles, leading to fracture.

In the present work, material properties, size and volume fraction of particles are given in Table 1. The quantity  $E$  denotes the Young’s modulus,  $\nu$  denotes the Poisson ratio,  $d$ ,  $\varphi$  are the average diameter and volume fraction of particles, respectively, and  $\hat{\sigma}$  is the interfacial strength between particles and matrix. The superscripts “p” and “s” denote primary and secondary particles, respectively. Similarly, we introduce the properties of the matrix material in Table 2.  $E^m$ ,  $\nu^m$ ,  $\sigma_y^0$  and  $h$  are the Young’s modulus, Poisson’s ratio, initial yield stress and strain hardening parameter, respectively.

Table 1  
Material properties, size and volume fraction of particles

$E^p$ (GPa)	$\nu^p$	$d^p$ ( $\mu\text{m}$ )	$\phi^p$	$\hat{\sigma}^p$	$E^s$ (GPa)	$\nu^s$	$d^s$ ( $\mu\text{m}$ )	$\phi^s$	$\hat{\sigma}^s$
630	0.3	1	0.02	1.0	630	0.3	0.2	0.02	3.1

Table 2  
Material properties of the matrix material

$E^m$ (GPa)	$\nu^m$	$\sigma_y^0$ (GPa)	$h$
210	0.3	1.6	0.42

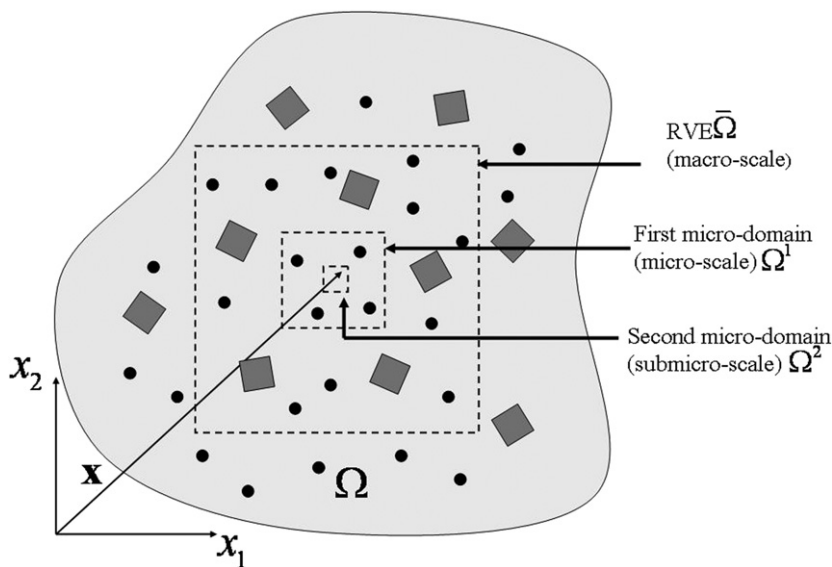


Fig. 2. Proposed multi-scale framework for the modeling of high strength steel showing the three nested domains centered at  $\mathbf{x}$ . The square shaped particles are primary particles and the circular inclusions are secondary particles.

### 2.2. Multi-scale decomposition of the microstructure

As noted above, ductile fracture in high strength steel alloys is a highly nonlinear phenomenon that encompasses several mechanisms across three scales: macro-scale, scale of primary particles, and scale of secondary particles. Following Vernerey et al. (2007) it is possible to associate to each scale of analysis an independent kinematic variable, arising from the introduction of material domains centered on a material point  $\mathbf{x}$ . The three kinematic variables and the associated nested domains shown in Fig. 2 are defined as follows:

- the macro-velocity  $\mathbf{v}$  is interpreted as the average velocity of the macro-domain  $\bar{\Omega}$ , a representative volume element of the entire microstructure. The characteristic dimension of  $\bar{\Omega}$  is a multiple of the average spacing between primary particles.
- the micro-velocity gradient  $\mathbf{L}^1$ , is interpreted as the average velocity gradient in the micro-domain  $\Omega^1$ , which represents the material between primary particles (secondary particles embedded in the matrix material).
- The submicro-velocity gradient  $\mathbf{L}^2$  is the average velocity gradient in the submicro-domain  $\Omega^2$ , which is representative of material between secondary particles (matrix material).

To simplify the description, we assume that the micro-domains  $\Omega^1$  and  $\Omega^2$  do not rotate relatively to the macroscopic domain. This is consistent with the fact that mechanisms of void growth do not involve significant rotation at small scales. Therefore, only effects of stretch and shear are considered at micro-scales and quantities  $\mathbf{L}^1$  and  $\mathbf{L}^2$  can be replaced by their symmetric counterparts, the rates of micro-deformation  $\mathbf{D}^1$  and submicro-deformation  $\mathbf{D}^2$  are written as follows:

$$\mathbf{D}^1 = \frac{1}{2}(\mathbf{L}^1 + (\mathbf{L}^1)^T) \text{ and } \mathbf{D}^2 = \frac{1}{2}(\mathbf{L}^2 + (\mathbf{L}^2)^T). \quad (1)$$

The generalized vector of strain rates is then written in the following form (Vernerey et al., 2007):

$$\Delta = [\mathbf{D} \quad (\mathbf{D}^1 - \mathbf{D}) \quad \mathbf{D}^1 \vec{\nabla} \quad (\mathbf{D}^2 - \mathbf{D}) \quad \mathbf{D}^2 \vec{\nabla}], \quad (2)$$

where  $\mathbf{D}$  is the rate of macro-deformation. The quantity  $\mathbf{D}^1 - \mathbf{D}$  (respectively,  $\mathbf{D}^2 - \mathbf{D}$ ) is the inhomogeneous deformation resulting from localization that occurs from void (respectively, microvoids) nucleation and growth. A generalized stress vector  $\Sigma$  can then be introduced as the power conjugate of  $\Delta$ . We write

$$\Sigma = \left[ \boldsymbol{\sigma} \quad \bar{\boldsymbol{\beta}}^1 \quad \bar{\bar{\boldsymbol{\beta}}}^1 \quad \bar{\boldsymbol{\beta}}^2 \quad \bar{\bar{\boldsymbol{\beta}}}^2 \right], \quad (3)$$

where  $\boldsymbol{\sigma}$  is the symmetric macro-stress (Cauchy stress),  $\bar{\boldsymbol{\beta}}^1$  and  $\bar{\bar{\boldsymbol{\beta}}}^1$  are the micro-stress and microscopic-stress couple and  $\bar{\boldsymbol{\beta}}^2$  and  $\bar{\bar{\boldsymbol{\beta}}}^2$  are submicro-stress and submicroscopic-stress couple. The micro-stresses and submicro-stresses are interpreted as stresses and stress moments exerted by the microstructure to redistribute plastic deformation around large voids and microvoids, respectively.

### 2.3. Internal power and governing equations

Introducing virtual kinematic quantities  $\delta v$ ,  $\delta \mathbf{D}^1$  and  $\delta \mathbf{D}^2$ , we show that the virtual internal power density of the three-scale micromorphic material can be written in the form (Vernerey et al., 2007):

$$\begin{aligned} \delta P_{\text{int}} &= \int_{\Omega} \Sigma \cdot \delta \Delta \, d\Omega \\ &= \int_{\Omega} \left\{ \boldsymbol{\sigma} : \delta \mathbf{D} + \bar{\boldsymbol{\beta}}^1 : \delta(\mathbf{D}^1 - \mathbf{D}) + \bar{\bar{\boldsymbol{\beta}}}^1 : \delta \mathbf{D}^1 \vec{\nabla} + \bar{\boldsymbol{\beta}}^2 : \delta(\mathbf{D}^2 - \mathbf{D}) + \bar{\bar{\boldsymbol{\beta}}}^2 : \delta \mathbf{D}^2 \vec{\nabla} \right\} d\Omega, \end{aligned} \quad (4)$$

where  $\delta \Delta$  is the generalized virtual strain rate. Confining attention to quasistatic case and denoting macroscopic body forces as  $\mathbf{b}$  and surface tractions as  $\mathbf{t}$ , it is straightforward to show (Vernerey et al., 2007) that the governing equations and boundary conditions are given by

$$\begin{aligned} (\boldsymbol{\sigma} - \bar{\boldsymbol{\beta}}^1 - \bar{\boldsymbol{\beta}}^2) \cdot \vec{\nabla} &= \mathbf{b} \text{ in } \Omega, & (\boldsymbol{\sigma} - \bar{\boldsymbol{\beta}}^1 - \bar{\boldsymbol{\beta}}^2) \cdot \mathbf{n} &= \mathbf{t} \text{ on } \Gamma_t, \\ \bar{\bar{\boldsymbol{\beta}}}^1 \cdot \vec{\nabla} - \bar{\boldsymbol{\beta}}^1 &= 0 \text{ in } \Omega, & \bar{\bar{\boldsymbol{\beta}}}^1 \cdot \mathbf{n} &= 0 \text{ on } \Gamma_t, \\ \bar{\bar{\boldsymbol{\beta}}}^2 \cdot \vec{\nabla} - \bar{\boldsymbol{\beta}}^2 &= 0 \text{ in } \Omega, & \bar{\bar{\boldsymbol{\beta}}}^2 \cdot \mathbf{n} &= 0 \text{ on } \Gamma_t. \end{aligned} \quad (5)$$

This is a system of three coupled differential equations, representing macro-, micro- and submicro-scales, respectively. The first equation represents the macroscopic equilibrium at a material point  $\mathbf{x}$ . The second and third equations are the equilibrium of stresses and stress couples arising at the micro- and submicro-scale at the same material point  $\mathbf{x}$ . Note that the micro-stresses  $\bar{\boldsymbol{\beta}}^1$  and  $\bar{\bar{\boldsymbol{\beta}}}^2$  provide interactions between each micro-scale and the macro-scale.

### 3. Constitutive relations

The constitutive relation relates the evolution of the generalized stress measure to the evolution of the generalized strain measure. In this work, the load carrying capacity of the material is characterized at various scales by a coupled elasto-plastic model. While the macro-scale material response is based on traditional

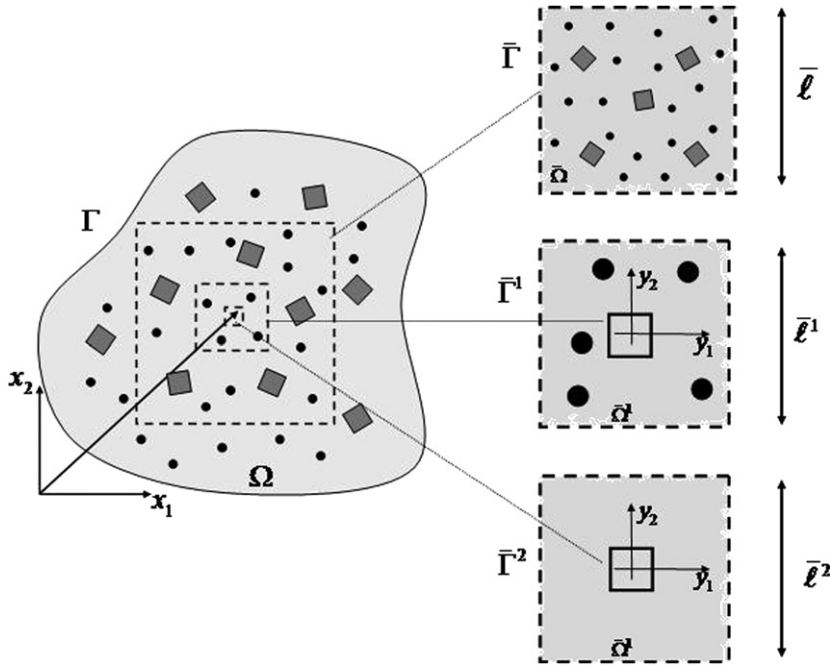


Fig. 3. Framework for the three-scale homogenization of high strength steel.

homogenization techniques (Nemat-Nasser and Hori, 1999; Hao et al., 2004), the micro-scales are based on an averaging operation described below.

### 3.1. Averaging operation

At the micro-scales, homogenization operations are based on the introduction of meso-domains  $\bar{\Omega}^I (I = 1, 2)$  associated with each micro-scale and centered on the material point  $\mathbf{x}$ . The dimensions  $\bar{\ell}^I$  of the meso-domains  $\bar{\Omega}^I$  are such that the micro-velocity gradient  $L^I$  varies linearly in  $\bar{\Omega}^I$  and  $\bar{\ell} \gg \bar{\ell}^1 \gg \bar{\ell}^2$ , where  $\bar{\ell}$  is the dimension of the macro-domain. Typically,  $\bar{\ell}^I$  is a multiple of the dimension of the micro-domain  $\Omega^I$ .

Fig. 3 gives an illustration of the macro-domain  $\bar{\Omega}$  and two meso-domains  $\bar{\Omega}^1$  and  $\bar{\Omega}^2$ . The length  $\bar{\ell}^1$  is related to the linear variation of inhomogeneous strain around the voids that directly depends upon their sizes. For simplicity, we assume that  $\bar{\ell}^1$  remains constant during deformation and we choose it as the average diameter of the primary particles. Similar arguments are used to choose the length scale  $\bar{\ell}^2$  as the average diameter of secondary particles. The next step in the homogenization (can also be interpreted as a statistical averaging operator) at micro-scales is the introduction of inhomogeneous micro-stress  $\boldsymbol{\beta}^1$  and submicro-stress  $\boldsymbol{\beta}^2$ ; these are power conjugates of the inhomogeneous deformations  $\mathbf{D}^1 - \mathbf{D}$  and  $\mathbf{D}^2 - \mathbf{D}$ , respectively. The homogenization procedure consists of replacing the stress field  $\boldsymbol{\beta}^I (I = 1, 2)$  in the meso-domain by an equivalent stress  $\bar{\boldsymbol{\beta}}^I (I = 1, 2)$  and stress couple  $\bar{\boldsymbol{\beta}}^I (I = 1, 2)$  as follows. Let  $\mathbf{y}$  be the position of a point in  $\bar{\Omega}^I (I = 1, 2)$  with respect to its center. The components of stress  $\bar{\boldsymbol{\beta}}^I (I = 1, 2)$  and stress couple  $\bar{\boldsymbol{\beta}}^I (I = 1, 2)$  are then given by the zeroth and first (statistical) moments of the stress  $\boldsymbol{\beta}^I (I = 1, 2)$  in the meso-volume  $\bar{\Omega}^I$  (Vernerey et al., 2007):

$$\bar{\boldsymbol{\beta}}^I(\mathbf{x}) = \frac{1}{\bar{\Omega}^I} \int_{\bar{\Omega}^I} \boldsymbol{\beta}^I(\mathbf{x} + \mathbf{y}) d\bar{\Omega}^I \quad (I = 1, 2). \tag{6}$$

$$\bar{\boldsymbol{\beta}}^I(\mathbf{x}) = \frac{1}{\bar{\Omega}^I} \int_{\bar{\Omega}^I} \boldsymbol{\beta}^I(\mathbf{x} + \mathbf{y}) \otimes \mathbf{y} d\bar{\Omega}^I$$

Note that this operation introduces length scales  $\bar{\ell}^1$  and  $\bar{\ell}^2$  in the model and can be interpreted through Eq. (6) as a measure of the lever arm of the stress couples.

### 3.2. Elastic response

In this study, an additive decomposition of the generalized rate of deformation into an elastic part  $\Delta^e$  and a plastic part  $\Delta^p$  is assumed:

$$\Delta = \Delta^p + \Delta^e. \quad (7)$$

For damage models, elastic strains usually remain small compared to plastic strains and a linear hypo-elastic response can therefore be assumed in the elastic regime. The relationship between an objective rate (Jaumann rate) of generalized stress  $\Sigma^\nabla$  and the generalized elastic rate of deformation  $\Delta^e$  can thus be written

$$\begin{bmatrix} \sigma \\ \bar{\beta}^1 \\ \bar{\beta}^1 \\ \bar{\beta}^2 \\ \bar{\beta}^2 \end{bmatrix}^\nabla = \begin{bmatrix} \bar{\mathbf{C}} & \mathbf{0} & \mathbf{0} & \mathbf{0} & \mathbf{0} \\ \mathbf{0} & \bar{\mathbf{C}}^1 & \bar{\mathbf{B}}^1 & \mathbf{0} & \mathbf{0} \\ \mathbf{0} & \bar{\mathbf{B}}^1 & \bar{\mathbf{C}}^1 & \mathbf{0} & \mathbf{0} \\ \mathbf{0} & \mathbf{0} & \mathbf{0} & \bar{\mathbf{C}}^2 & \bar{\mathbf{B}}^2 \\ \mathbf{0} & \mathbf{0} & \mathbf{0} & \bar{\mathbf{B}}^2 & \bar{\mathbf{C}}^2 \end{bmatrix} \cdot \begin{bmatrix} \mathbf{D} \\ \mathbf{D}^1 - \mathbf{D} \\ \mathbf{D}^1 \bar{\nabla} \\ \mathbf{D}^2 - \mathbf{D} \\ \mathbf{D}^2 \bar{\nabla} \end{bmatrix}^e, \quad (8)$$

where  $\bar{\mathbf{C}}$  is the macroscopic elastic matrix,  $\bar{\mathbf{C}}^1, \bar{\mathbf{C}}^2$  and  $\bar{\mathbf{B}}^1$  are the microscopic elastic matrices and  $\bar{\mathbf{C}}^2, \bar{\mathbf{C}}^1$  and  $\bar{\mathbf{B}}^2$  are the submicroscopic elastic matrices. Note that the zeros on the off-diagonal matrices arise from the assumption that coupling terms between deformations at different scales are negligible in the elastic regime. Some relationships between elastic matrices can be determined from averaging operations on the meso-domains defined in Eq. (6). For this, let us assume that within the meso-domain  $\bar{\Omega}^I$ , the stress rate  $\beta^{I,\nabla}$  is related to the quantity  $\mathbf{D}^I - \mathbf{D}$  through a local elastic matrix  $\mathbf{C}^I$  as follows:

$$\beta^{I,\nabla}(\mathbf{x} + \mathbf{y}) = \mathbf{C}^I : [\mathbf{D}^I(\mathbf{x} + \mathbf{y}) - \mathbf{D}(\mathbf{x})]^e. \quad (9)$$

Assuming that the elastic matrix  $\mathbf{C}^I$  remains constant within the meso-domain  $\bar{\Omega}^I$ , it is straightforward to show, using Eq. (6), that the elastic moduli  $\bar{\mathbf{C}}^I (I = 1, 2)$  and  $\bar{\mathbf{C}}^I (I = 1, 2)$  can be written in the following form:

$$\bar{\mathbf{C}}^I = \mathbf{C}^I, \quad \bar{\mathbf{C}}^I = \frac{\bar{\ell}^I}{12} \mathbf{C}^I \otimes \mathbf{I} \quad \text{and} \quad \bar{\mathbf{B}}^I = \mathbf{0}. \quad (10)$$

In the present study, the values of elastic constants that appear in  $\mathbf{C}^I (I = 1, 2)$  are phenomenological and their determination is left for future work. However, the best agreement between cell model computation and multi-scale continuum simulations was obtained for  $\mathbf{C}^1 = \mathbf{C}^2 \approx \frac{1}{10} \mathbf{C}$  where  $\mathbf{C}$  is the macroscopic elastic matrix. A more elaborate representation of the elastic response at micro-scales could employ cell modeling techniques and is the subject of future research. We now introduce the plastic constitutive response associated with macro-, micro- and submicro-scales.

### 3.3. Plastic response

The material response in the plastic range is represented by a three-potential plasticity model. In other words, the constitutive relations involve three yield functions  $\Phi(\sigma, \mathbf{Q})$ ,  $\Phi^1(\bar{\beta}^1, \bar{\beta}^1, \mathbf{Q})$  and  $\Phi^2(\bar{\beta}^2, \bar{\beta}^2, \mathbf{Q})$  associated with macro-, micro- and submicro-scale, respectively. The quantity  $\mathbf{Q}$ , called the vector of internal variables, represents a measure of the state of the microstructure (such as damage) at a material point. In our model,  $\mathbf{Q}$  consists of the macroscopic plastic deformation  $\varepsilon_p$ , porosity  $f$ , microscopic and submicroscopic plastic deformation  $E^1$  and  $E^2$ , respectively,

$$\mathbf{Q} = [\varepsilon_p \quad f \quad E^1 \quad E^2]^T. \quad (11)$$

In the following, we present a derivation of the yield function and an evolution of internal variables associated with each scale, starting at the macro-scale. While the macroscopic plastic response is determined based on hierarchical homogenization techniques described in Hao et al. (2004), the microscopic and submicroscopic constitutive relations remain empirical but physically motivated.

Note that although the material’s microstructure is typically anisotropic and discontinuous at small scales, we assume that the above yield functions are isotropic and continuous for simplicity. The extension of this work to anisotropic, non-smooth yield criteria will be considered in future work.

### 3.3.1. Macroscopic plastic response

The macro-scale material response reflects the overall material behavior for dimensions that are much larger than the microstructure’s characteristic length. At this scale, the plastic deformation and damage is the result from plastic slip in the matrix and void nucleation and growth around both primary and secondary particles. Due to the weak bonding between primary particles and the matrix material, voids nucleate first and grow around the primary particles, creating bands of intense plastic strains. At sufficiently large strains, microvoids nucleate and grow from secondary particles within these bands, triggering the so-called “void-sheet mechanism” between larger voids. This mechanism was investigated by Tvergaard (1982, 1988). Thus, in addition to the effect of void nucleation and growth from primary particles, the macroscopic yield criterion must incorporate the effect of microvoid nucleation along with their growth and coalescence. Motivated by the work of Perrin and Leblond (2000), the macroscopic yield function  $\Phi$  is assumed to be Gurson-type in which the porosity is modified to account for voids nucleating from primary and secondary particles. Hence, the yield function is written in terms of three material parameters  $q_1$ ,  $q_2$  and  $q_3$  as (Table 3) follows:

$$\Phi = \left(\frac{\sigma_{eq}}{\sigma_y}\right)^2 - 1 + 2q_1 f \cosh\left(\frac{3q_2 \sigma_m}{2\sigma_y}\right) - q_3 f^2 = 0, \tag{12}$$

where the yield stress  $\sigma_y$  evolves with the level of plastic strain, measured by the scalar quantity  $\varepsilon_p$  and the scalar  $f$  accounts for the porosity resulting from both voids and microvoids. We write

$$f = f^p + f^s, \tag{13}$$

where  $f^p$  and  $f^s$  represent the porosity due to voids and microvoids, respectively. Note that the porosity  $f^s$  is introduced to characterize the rapid failure of the material after the microvoid nucleation and is an effective porosity that does not represent the average volume fraction of microvoids in a macroscopic volume. The evolution equations for the macrosopic internal variables  $f$  and  $\varepsilon_p$  have the form:

$$\begin{cases} \dot{\varepsilon}_p = [\boldsymbol{\sigma} : \mathbf{D}^p]/[(1-f)\sigma_{eq}], \\ \dot{f} = \dot{f}^s + \dot{f}^p, \text{ where } \begin{cases} \dot{f}^p = \dot{f}^n + \dot{f}^g, \\ \dot{f}^s = \dot{f}^c, \end{cases} \end{cases} \tag{14}$$

where  $\dot{f}^n, \dot{f}^g$  denote the rate of increase of porosity from nucleation and growth of voids around primary particles while  $\dot{f}^c$  accounts for void coalescence resulting from the void-sheet mechanism. Further details are given in Appendix A.

*Note:* The authors acknowledge that the model given by Eq. (12) has some limitation with regards to microstructural non-uniformity and anisotropy (Lee and Ghosh, 1999). However, it is a useful starting point for purposes of demonstrating the present multi-scale methodology. Improvements on this model will be considered in future research.

Table 3  
Material parameters used at the macroscale

$q_1$	$q_2$	$q_3$
0.91	1.9	0.95

### 3.3.2. Microscopic plastic response

The micro-stress and micro-stress couple are a result of inhomogeneous stresses induced by the growth of voids around primary particles. At this scale, plasticity is governed by the behavior of the material surrounding those voids, namely the matrix and secondary particles. Physically, the micro-stress and micro-stress couple yield at the onset of void-sheet formation (due to microvoid nucleation). Micro-stresses therefore yield at the onset of microvoid nucleation and microscopic plastic deformation arises from microvoid growth. In order to account for volumetric deformation in the mathematical formulation, we represent the micro-scale plasticity by a simple Drucker–Prager-type yield function in the form:

$$\Phi^1(\bar{\mathbf{p}}^1, \bar{\mathbf{p}}^1, \mathbf{Q}) = (B_{\text{eq}}^1 + \alpha B_m^1) - B_y^1 = 0, \quad (15)$$

where  $B_{\text{eq}}^1$  and  $B_m^1$  are equivalent and hydrostatic micro-stresses that are modified to account for the effects of higher order stresses:

$$B_{\text{eq}}^1 = \sqrt{\frac{3}{2} \bar{\mathbf{p}}^{1,\text{dev}} : \bar{\mathbf{p}}^{1,\text{dev}} + \left(\frac{a^1}{\bar{\ell}^1}\right)^2 \bar{\mathbf{p}}^{1,\text{dev}} : \bar{\mathbf{p}}^{1,\text{dev}}}, \quad (16)$$

$$B_m^1 = \sqrt{\bar{\beta}^{1,m} \bar{\beta}^{1,m} + \left(\frac{b^1}{\bar{\ell}^1}\right)^2 \bar{\mathbf{p}}^{1,m} \cdot \bar{\mathbf{p}}^{1,m}}.$$

The expressions for deviatoric stresses  $\bar{\mathbf{p}}^{1,\text{dev}}$  and  $\bar{\mathbf{p}}^{1,\text{dev}}$ , and hydrostatic stresses  $\bar{\beta}^{1,m}$  and  $\bar{\beta}^{1,m}$  are developed in Appendix B.2. The yield stress  $B_y^1$  is assumed to be a function of the microscopic effective plastic strain  $E^1$  whose time derivative  $\dot{E}^1$  is taken to be

$$\dot{E}^1 = \sqrt{\frac{2}{3} (\mathbf{D}^{1,p} - \mathbf{D}^p) : (\mathbf{D}^{1,p} - \mathbf{D}^p) + c^1 \bar{\ell}^1 \mathbf{D}^{1,p} \vec{\nabla} : \mathbf{D}^{1,p} \vec{\nabla}}. \quad (17)$$

The coefficients  $a^1$ ,  $b^1$  and  $c^1$  are material parameters determined through the averaging operation (6) and are summarized in Table 4. Details of the calculation are given in Appendix B.

*Note:* the form of the flow potential in Eq. (15) was not derived from homogenization techniques and can certainly be improved upon for a better description of the material behavior. However, it captures the main features of mechanisms observed at this scale. Future research would involve the determination of flow potentials from homogenization techniques and consideration of anisotropy and probabilistic effects at microscopic scales.

The evolution of the microscopic effective plastic strain follows from the equality of plastic work:

$$[B_{\text{eq}}^1 + \alpha B_m^1] \dot{E}^1 = \bar{\mathbf{p}}^1 : (\mathbf{D}^1 - \mathbf{D})^p + \bar{\mathbf{p}}^1 : \mathbf{D}^{1,p} \vec{\nabla} \quad (18)$$

which leads to the relation

$$\dot{E}^1 = \frac{\bar{\mathbf{p}}^1 : (\mathbf{D}^1 - \mathbf{D})^p + \bar{\mathbf{p}}^1 : \mathbf{D}^{1,p} \vec{\nabla}}{B_{\text{eq}}^1 + \alpha B_m^1}. \quad (19)$$

As described in the previous section, the microscopic plastic flow is the result of microvoid nucleation and growth. The initial microscopic yield stress therefore corresponds to the onset of a void-sheet mechanism for which a criterion is given in Eq. (A.16), namely:

$$\varepsilon_p + a_{\text{vs}} f = b_{\text{vs}} (\sigma^s), \quad (20)$$

Table 4  
Material parameters used at the microscale

$a^1$	$b^1$	$c^1$	$\bar{\ell}^1$ ( $\mu\text{m}$ )	$h^1$	$\alpha$
18	$6\sqrt{6}$	1/18	1	0	1

where  $b_{vs}$  is a function of the debonding stress  $\hat{\sigma}^s$ . At the onset of a void-sheet mechanism, micro-stresses lie on the yield surface, implying that  $\Phi^1 = 0$ . Using Eqs. (20) and (A.16), we can write

$$B_{y0}^1 = (B_{eq}^1 + \alpha B_m^1)|_{f+a_{vs}e_p=b_{vs}}. \quad (21)$$

For simplicity, we assume that  $B_y^1$  is a linear function of  $E^1$

$$B_y^1 = B_{y0}^1(1 + h^1 E^1). \quad (22)$$

The coefficient  $h^1$  remains an arbitrary constant and gives the sensitivity of micro-stress softening with the amount of micro-deformation. Computations have shown that the behavior of the solution exhibits insignificant variations when we modify the value of  $h^1$ . In the following, we consider perfect plasticity for the inhomogeneous response at the micro-scale; in other words, we choose  $h^1 = 0$ .

### 3.3.3. Submicroscopic plastic response

The submicro-stress and submicro-stress couples are a result of inhomogeneous stresses induced by microvoid growth. At this scale, plastic instability occurs when the matrix material fails to carry stress moments after the onset of microvoid coalescence (or instability of ligaments between microvoids). Submicroscopic plastic deformation can subsequently be defined as the plastic deformation of the matrix material after the onset of void coalescence (necking of ligament). The yield function is written in the form of  $J_2$  flow plasticity modified to account for the effects of higher order stresses:

$$\Phi^2(\bar{\mathbf{p}}^2, \bar{\bar{\mathbf{p}}}^2, \mathbf{Q}) = B_{eq}^2 - B_y^2 = 0, \quad (23)$$

where  $B_{eq}^2$  is the overall equivalent micro-stress and  $B_y^2$  is the micro-yield stress. The equivalent stress and rate of plastic micro-strain  $\dot{E}^2$  are written in the form:

$$B_{eq}^2 = \sqrt{\frac{3}{2} \bar{\mathbf{p}}^{2,dev} : \bar{\mathbf{p}}^{2,dev} + \left(\frac{a^1}{\ell^1}\right)^2 \bar{\bar{\mathbf{p}}}^{2,dev} : \bar{\bar{\mathbf{p}}}^{2,dev}}, \quad (24)$$

$$\dot{E}^2 = \sqrt{\frac{2}{3} (\mathbf{D}^{2,p} - \mathbf{D}^p) : (\mathbf{D}^{2,p} - \mathbf{D}^p) + b^2 \bar{\ell}^2 \mathbf{D}^{2,p} \vec{\nabla} : \mathbf{D}^{2,p} \vec{\nabla}},$$

where  $\bar{\mathbf{p}}^{2,dev}$  and  $\bar{\bar{\mathbf{p}}}^{2,dev}$  are deviatoric submicro-stress and submicro-stress couple and  $a^2$  and  $b^2$  are material constants determined in Appendix B.1. The equality of plastic work implies that the increment of submicroscopic effective plastic strain takes the form:

$$\dot{E}^2 = \frac{\bar{\mathbf{p}}^2 : (\mathbf{D}^{2,p} - \mathbf{D}^p) + \bar{\bar{\mathbf{p}}}^2 : \mathbf{D}^{2,p} \vec{\nabla}}{B_{eq}^2}. \quad (25)$$

Here, the yield stress  $B_y^2$  is taken as the value of equivalent stress  $B_{eq}^2$  at the onset of microvoid coalescence. A measure of inhomogeneous plastic deformation in the inter-void ligament is provided by the effective plastic micro-strain  $E^1$ . The critical plastic micro-strain at microvoid coalescence is denoted by  $E_c^1$  and the yield stress  $B_{y0}^2$  can be written as

$$B_{y0}^2 = B_{eq}^2|_{E^1=E_c^1}. \quad (26)$$

The value of  $E_c^1$  can be interpreted as the microscopic plastic strain at the onset of microvoid coalescence. This value was evaluated by measuring the plastic strain in a unit cell in uniaxial tension at onset of microvoid coalescence. Perfect plasticity is also used at the submicro-scale ( $B_y^2$  remains constant,  $B_y^2 = B_{y0}^2$ ). Summaries of constitutive relations and homogenization techniques used in this section are given in Figs. 4 and 5.

### 3.4. A hierarchical scheme for the macroscopic plastic response

In this section, we describe the framework that is used to determine the macroscopic yield function  $\Phi$ . This is done by using concepts from the hierarchical framework (Hao et al., 2004) and cell modeling

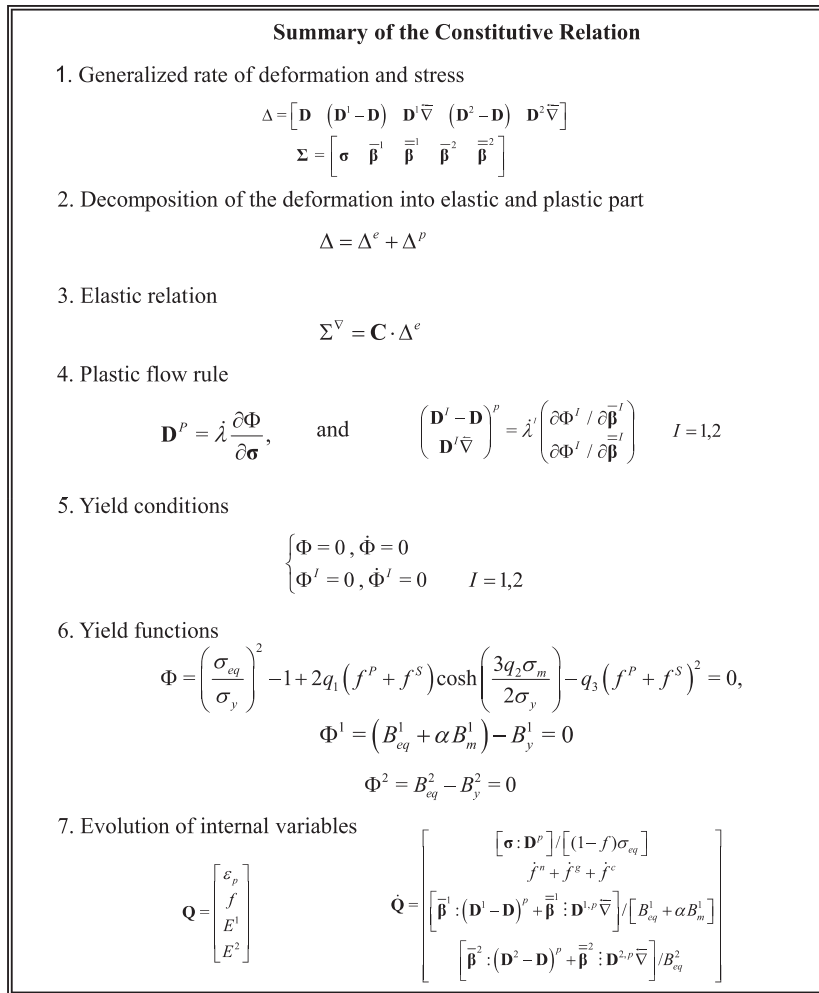


Fig. 4. Summary of the constitutive relation.

techniques. One of the critical feature to capture from cell modeling is the strength of the interface between particles and matrix material. For this, we used the cohesive model described next.

3.4.1. Matrix/particles cohesive law

The interfacial debonding energy at Fe–TiC interface for secondary particles and Fe–TiN interface for primary particles is modeled by a force–separation relation obtained from first principle calculations (Freeman, 2002; Geng et al., 2001). Let  $\sigma$  be the normal stress across the interface and  $\delta$  be the separation between the two surfaces. The force–separation relation is written in the non-dimensional form as

$$\frac{\sigma}{\hat{\sigma}} = \frac{\delta}{\hat{\delta}} \exp \left( 1 - \frac{\delta}{\hat{\delta}} \right), \tag{27}$$

where  $\hat{\sigma}$  is the peak debonding stress and  $\hat{\delta}$  is the separation when  $\sigma = \hat{\sigma}$ . The peak debonding stresses at the primary particle/matrix interface and secondary particle/matrix interface are denoted by  $\hat{\sigma}^p$  and  $\hat{\sigma}^d$ , respectively. In the present work, a scaling of the force–separation relation (27) is necessary so that the results from quantum mechanics can be used in a continuum framework at the particle scale. For this, we refer to Hao et al. (2004), where the force–separation relation is scaled based on dislocation pile-up at particle boundaries.

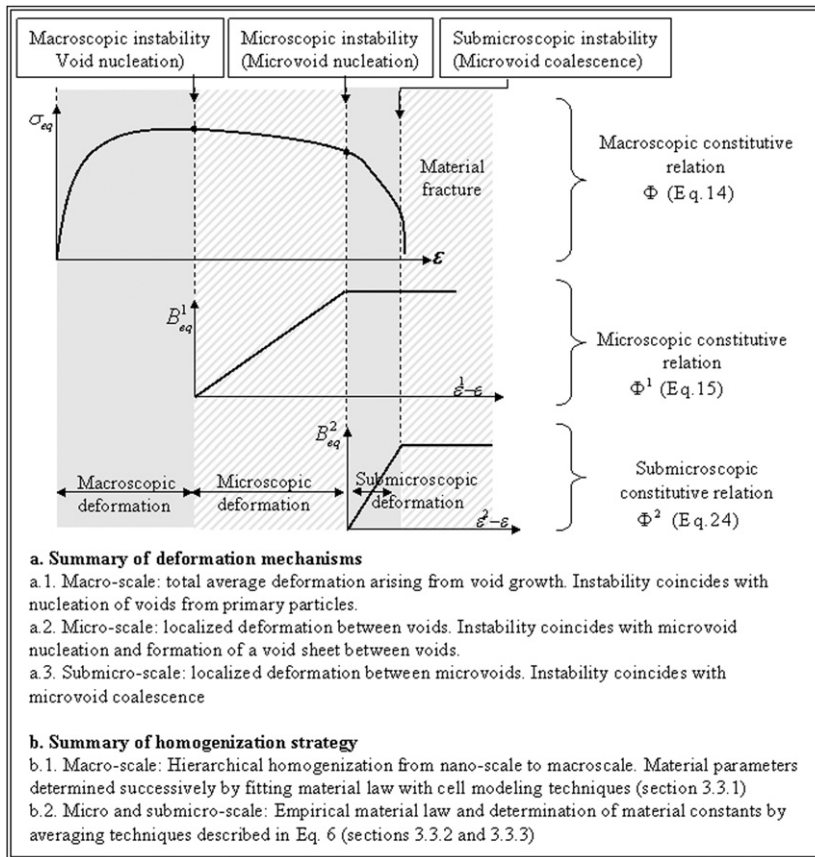


Fig. 5. Summary of the model and homogenization.

### 3.4.2. Hierarchical homogenization

The hierarchical framework used in this study is depicted in Fig. 6. Homogenization of the material at the level of secondary particles is first carried out to produce a homogenized constitutive relation that can be used to model the material between primary particles. A cell model at the scale of primary particles is then used to determine properties of the material at the macro-scale. At each scale, we introduce a representative cell  $\Omega$  in which homogenization procedures are performed. These operations provide a relationship between average quantities  $(\boldsymbol{\sigma}, \mathbf{D})$  in  $\Omega$  and local quantities  $(\tilde{\boldsymbol{\sigma}}, \tilde{\mathbf{D}})$ :

$$\boldsymbol{\sigma} = \frac{1}{\Omega} \int_{\Omega} \tilde{\boldsymbol{\sigma}} \, d\Omega, \quad \mathbf{D} = \frac{1}{\Omega} \int_{\Omega} \tilde{\mathbf{D}} \, d\Omega. \quad (28)$$

The quantities  $\boldsymbol{\sigma}$  and  $\tilde{\boldsymbol{\sigma}}$  are average and local Cauchy stresses, respectively, and  $\mathbf{D}$  and  $\tilde{\mathbf{D}}$  are average and local rates of deformation. At each scale, the plastic behavior is determined by assuming a form for the yield function for which material parameters are determined by curve fitting the response given by the cell model.

The determination of a constitutive relation at the level of secondary particles is first carried out to generate a model that is used for the matrix material in the macroscale. At this scale, we introduce an RVE that consists of a domain that contains several randomly located particles as represented in Fig. 6 (plotted with contours of equivalent plastic strain) and apply periodic boundary conditions described in Appendix C.

At the scale of secondary particles, the failure mechanisms of the material depend on the level of triaxiality. In high triaxiality, they are explained by microvoid nucleation around secondary particles, growth and coalescence. In low triaxiality, the softening arises from coalescence of neighboring microvoids that lie in the direction of shear (McVeigh et al., 2007; Vernerey et al., 2006). As described in McVeigh et al. (2007), the effect of these micro-mechanisms on the evolution of average stress state can be represented by a Gurson-type

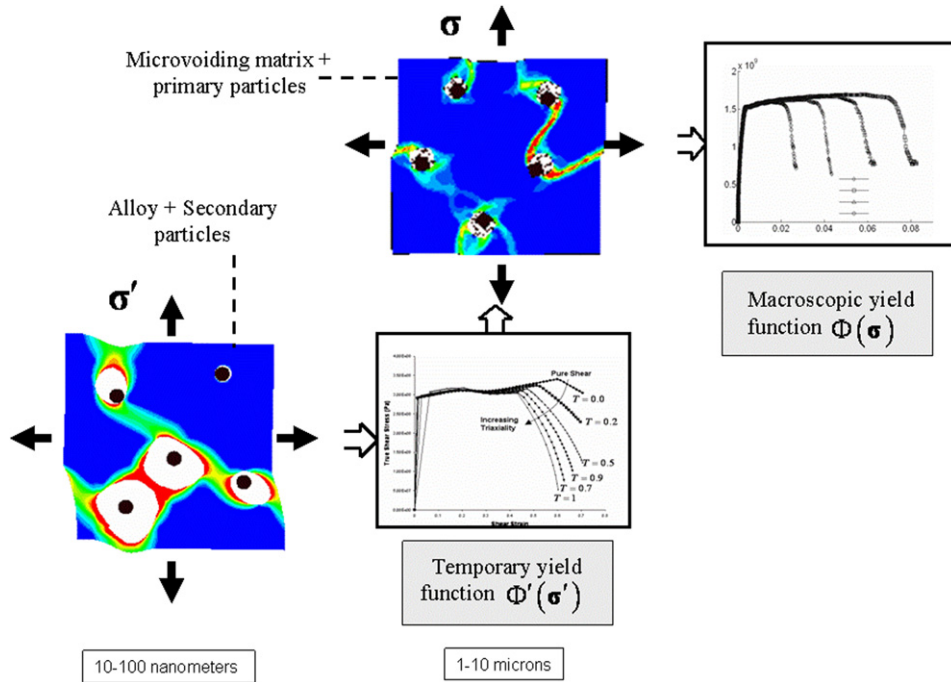


Fig. 6. Hierarchical framework for the determination of the macroscopic constitutive relation.

plastic potential  $\Phi'$  (Gurson, 1977) with adjustable parameters as follows:

$$\Phi' = \left( \frac{\sigma'_{\text{eq}}}{\sigma_y} \right)^2 + 2q'_1 f' \cosh \left( \frac{3q'_2 \sigma'_m}{2\sigma_y} \right) - (1 + q'_3 (f')^2) = 0, \quad (29)$$

where the prime denotes the scale of secondary particles. Here,  $\sigma'_m$  is the hydrostatic stress and  $\sigma'_{\text{eq}}$  is the equivalent stress. The determination of constants  $q'_1$ ,  $q'_2$  and  $q'_3$  is described in Appendix C. The evolution of the microvoid volume fraction  $f'$  is decomposed into a nucleation term, growth term and coalescence term. The evolution of each of these internal variables is described in Appendix A.1. Note that the function  $\Phi'$  is only used temporarily in order to determine the macroscopic material response. It is not used in the multi-scale framework described in previous sections.

The macroscale yield function is then determined by considering the unit cell containing a distribution of randomly distributed primary particles in a matrix whose response is given by Eq. (29). A similar averaging operation is performed to lead to the form of the yield function (12) and the evolution of internal variables given in Eq. (14).

## 4. Implemented multi-scale model results

### 4.1. One-dimensional analysis

The behavior of the three-scale micromorphic steel model is first investigated in a simple one-dimensional case. Consider a rectangular bar, which is stretched such that the ends move at velocity  $v$  in opposite directions. The geometry, dimensions and boundary conditions are depicted in Fig. 7.

An imperfection is introduced in the center of the bar in order to trigger the onset of localization within this region. This is done by assigning a 5% reduction of the initial yield stress in the central element. In order to compute the solution accurately, the element size has to be comparable to the smallest length scale  $\bar{\ell}^2$  (0.2  $\mu\text{m}$ ).

4.1.1. Three-scale continuum solution

In Fig. 8, the evolution of the profile of macroscopic logarithmic tensile strain is plotted as a function of position along the bar. Each of the three distinct stages is observed in failure of the bar based on the size of the corresponding localization region.

- Stage 1 corresponds to localization of the deformation as a result of macroscopic material instability (due to the nucleation of voids from primary particles in the center of the bar). The width of the localization zone is due to micro- and micro-stress couple that are associated with the length scale  $\bar{\ell}^1$ .
- Stage 2 corresponds to the second level of localization, associated with microscopic instability. At this stage, due to sufficient plastic strains and voids growth around the primary particles, microvoid nucleation takes place, leading to a microvoid sheet. The width of the localization zone is due to submicro-stress and submicro-stress couple that are associated with length scale  $\bar{\ell}^2$  given by secondary particles (Table 5).

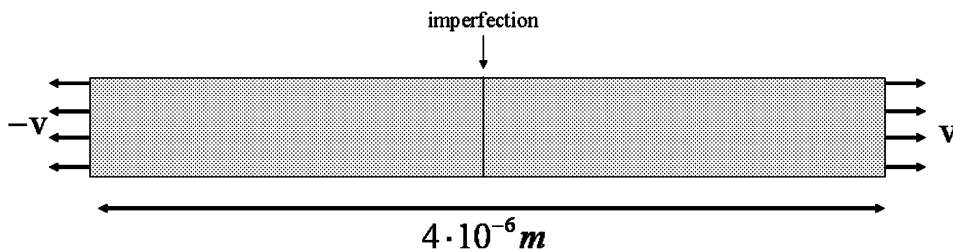


Fig. 7. One-dimensional tensile bar.

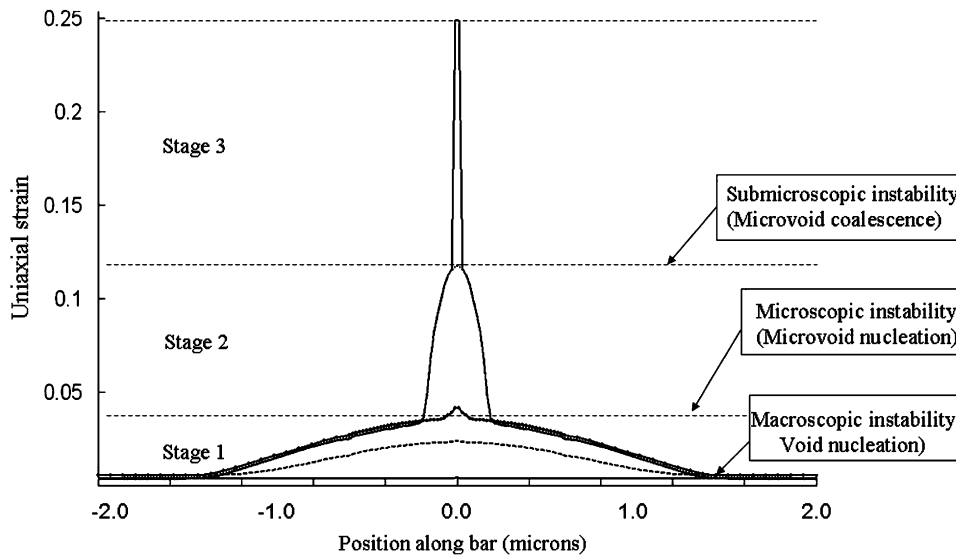


Fig. 8. Logarithmic tensile strain profile for different stages of deformation.

Table 5  
Material parameters used at the submicro-scale

$a^2$	$b^2$	$\ell^2$ ( $\mu\text{m}$ )	$h^2$	$E_c^1$
18	$6\sqrt{6}$	0.2	0	1

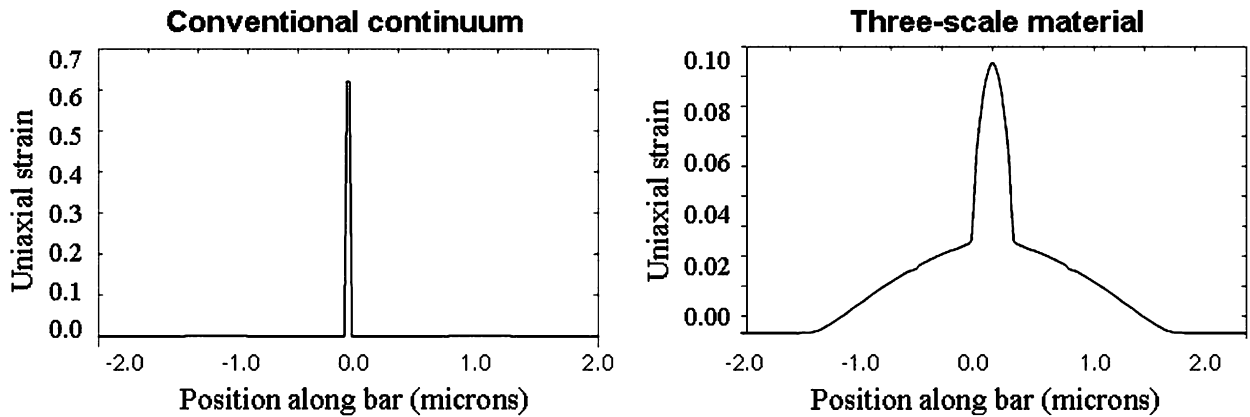


Fig. 9. Solutions for conventional continuum and multi-scale continuum.

- Finally, stage 3 is associated with final failure of the material due to microvoid coalescence. This occurs when submicro-stresses and stress couples reach the submicroscopic yield surface. At this stage, size effects are no longer present and the solution becomes element-size dependent.

The three-scale micromorphic model therefore has the ability to accurately capture several instability points during material failure, as well as the characteristic sizes of localization regions. This represents an appreciable improvement from conventional continuum theories that failed in predicting post-localization behavior of materials. For comparison, Fig. 9 depicts the solution given for a conventional continuum (one-scale) and three-scale continuum solution. For the conventional continuum model, the constitutive relation consists of macroscopic elastic constants and the macroscopic yield function developed in this paper.

Because it is a local model, the conventional continuum exhibits spurious strain localization after reaching material instability. On the contrary, the multi-scale material model correctly captures the three stages of ductile failure of steel: void nucleation and growth, microvoid nucleation and growth, and finally, microvoid coalescence.

#### 4.1.2. Effect of particle size

The effect of particle size is investigated for the one-dimensional problem. In Fig. 10(a), we vary the size of primary particles. The consequence is a change in size of the plastic region at the micro-scale. However, no change is observed in the localization zone at the submicro-scale. On the contrary, varying the size of secondary particles has an affect on the size of the plastic region at the submicro-scale but no impact on the localization zone at the micro-scale (shown in Fig. 10(b)). It is clear that secondary particles size only has an influence on the size of the plastic region due to void-sheet mechanism. This emphasizes the relationship between failure mechanisms and their associated length scales.

#### 4.1.3. Effect of the carbide/matrix debonding stress

We now investigate the effect of debonding peak stress  $\hat{\sigma}^s$  between secondary particles and matrix material. The tensile strain profiles are plotted for different values of  $\hat{\sigma}^s$  in Fig. 10(c). The figure clearly shows that increasing the debonding stress has the effect of delaying localization of deformation at the scale of secondary particles. This is a direct consequence of the criterion for void sheet driven coalescence given in Eq. (A.16).

### 4.2. Two-dimensional shear problem

Next, a two-dimensional plane strain finite element analysis of a shear test is performed to evaluate the performance of the three-scale micromorphic model with respect to localization in shear conditions. The geometry and boundary conditions shown in Fig. 11(a) are motivated by the experiments of Cowie et al. (1989) (although the region considered here is smaller than the gage section in experiments).

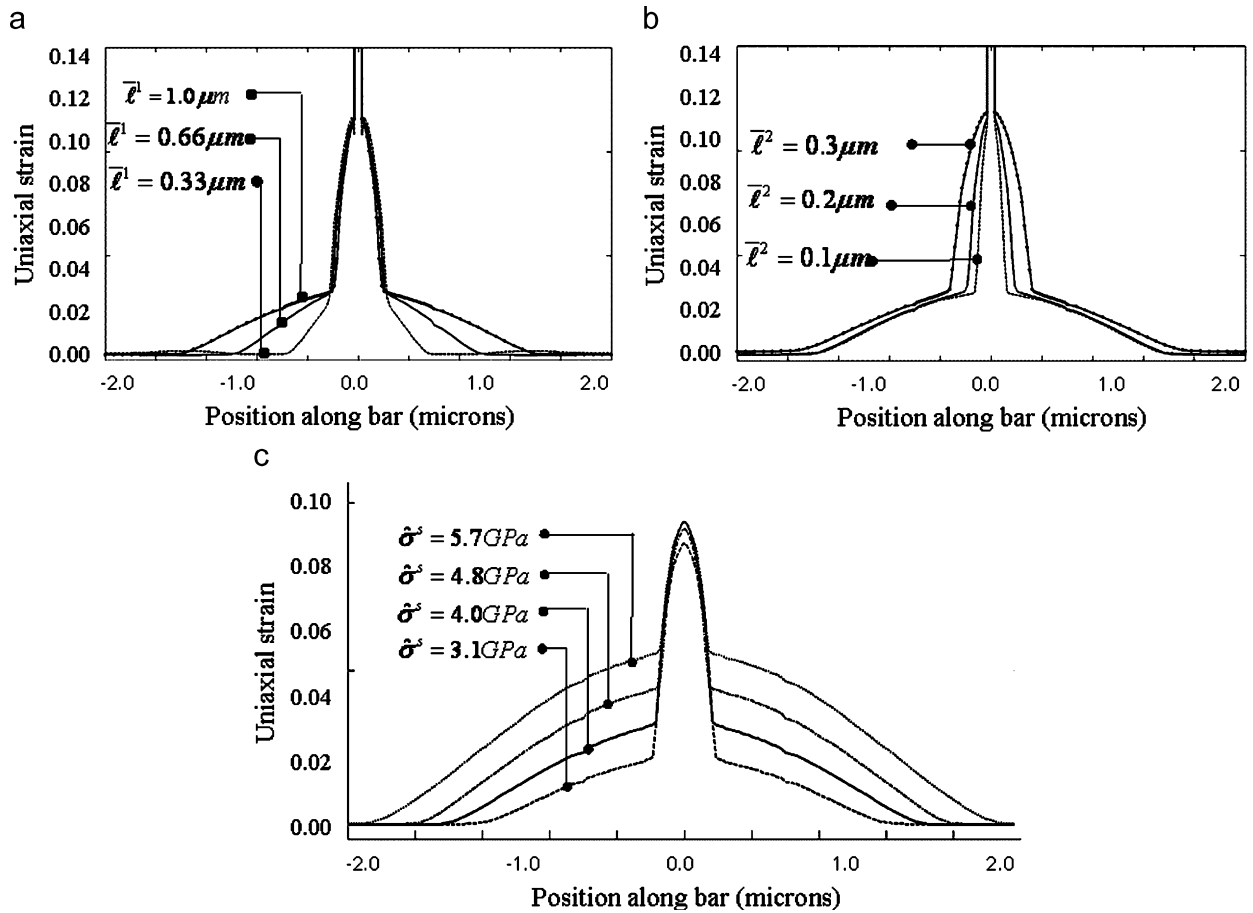


Fig. 10. Profile of tensile strains for different particle sizes: (a) effect of the primary particles size; (b) effect of secondary particles size; and (c) effect of debonding peak stress at TiC–Fe interface (secondary particles).

Two computations are performed. First, a direct numerical simulation (DNS) of the shear test with explicit modeling of two populations of particles and second, a computation of the equivalent three-scale micromorphic model. For DNS to be computationally affordable, the size of the shear specimen is scaled down to micron size. Yet, due to the small size of secondary particles ( $0.1 \mu\text{m}$ ), the typical size of an element is  $10 \text{ nm}$ . Fig. 11(b) shows the finite element discretization used for the DNS in which eight primary particles and 22 secondary particles can be distinguished. To reduce the computation size, we only modeled secondary particles at the center of the specimen where failure is expected. The simulation is carried out with the ABAQUS<sup>®</sup> finite element software, using 59,394 quadrilateral plane strain elements.

The finite element discretization for the multi-scale micromorphic simulation is shown in Fig. 11(c). To capture submicroscopic fields, the element size has to be comparable to  $\bar{\ell}^2$  ( $0.1 \mu\text{m}$ ). Similar to DNS, the discretization is refined in the center of the specimen that permits to reduce the number of quadrilateral element to 892. The comparison between distribution of effective plastic strains at different times for both DNS and three-scale micromorphic model is presented in Fig. 12.

The three stages of shear failure described above can be observed:

- Stage 1: Void nucleation and localization of plastic deformation in a shear band between newly created voids of width  $\bar{\ell}^1$ . This corresponds to macroscopic instability.
- Stage 2: Microvoid nucleation and localization of plastic deformation in a band of width  $\bar{\ell}^2$  between microvoids. This corresponds to microscopic instability.
- Stage 3: Onset of microvoid coalescence and submicroscopic instability.

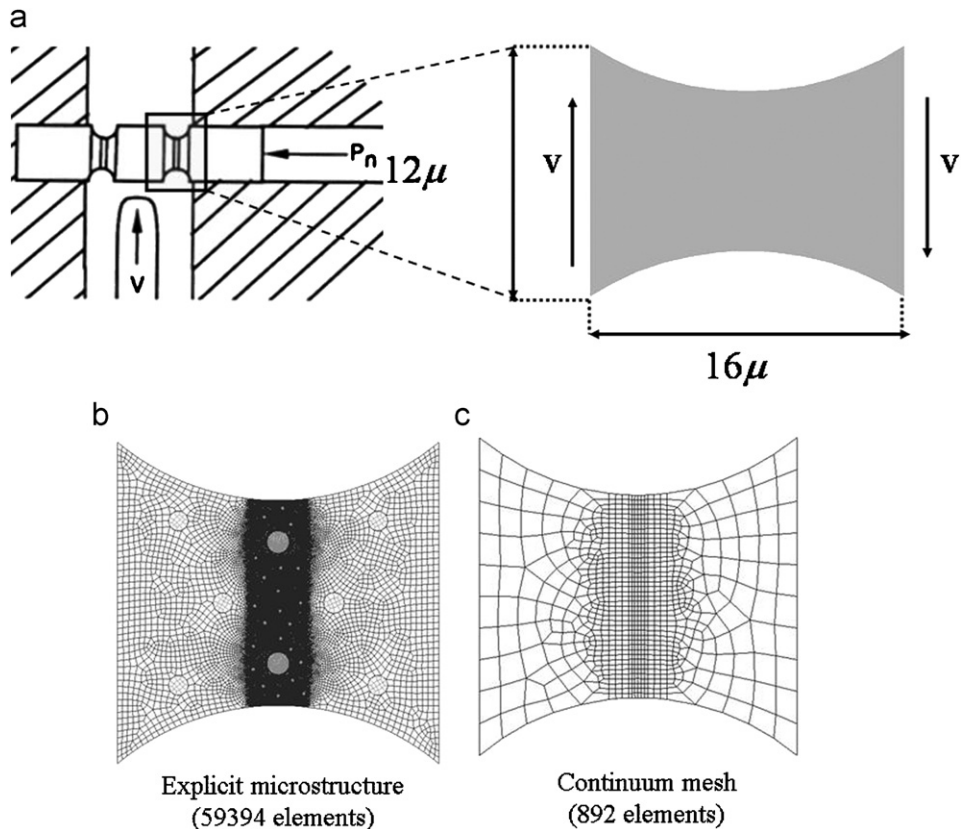


Fig. 11. (a) Setting of the shear test experiment and finite element discretization used for (b) simulation with explicit microstructure and (c) three-scale micromorphic model.

The evolutions of microscopic and submicroscopic shear stresses are depicted in Fig. 12(c) and (d). The microscopic shear stress represents a couple that distributes strains in a band whose size is given by primary particles. It is active in stage 1 but yields during microscopic instability, as microvoids nucleate. During stage 1, the submicro-stresses remain insignificant since the deformation is microscopic. However, they become fully active after microscopic instability and finally yield in stage 3 due to microvoids coalescence.

The three-scale micromorphic model was able to provide an accurate description of various failure mechanisms with their length scales. We now show how macroscopic response for the DNS compares to that of the multi-scale model by plotting the average stress–strain curve in the specimen depicted in Fig. 13.

A good agreement between the two simulations is observed. The oscillations of the stress–strain curve of the DNS are due to the existence of the explicit microstructure whose length scale is close to specimen size. These oscillations would diminish if a larger specimen is considered.

#### 4.3. Two-dimensional tensile test

The three-scale model is now evaluated with a finite element analysis of a specimen in tension under plane strain conditions. Consider a square domain subject to tension by applying a velocity  $v$  on top and bottom boundaries in opposite directions, as shown in Fig. 14(a). To start the localization, an imperfection is introduced at the center of the domain by giving the central element a 5% reduction in yield stress.

Using the symmetric geometry of the domain, the problem is reduced to the study of the quarter cell and boundary conditions shown in Fig. 14(b). The domain is discretized with 4121 quadrilateral elements whose size compare to the length scale  $\ell^*$  of the secondary particles.

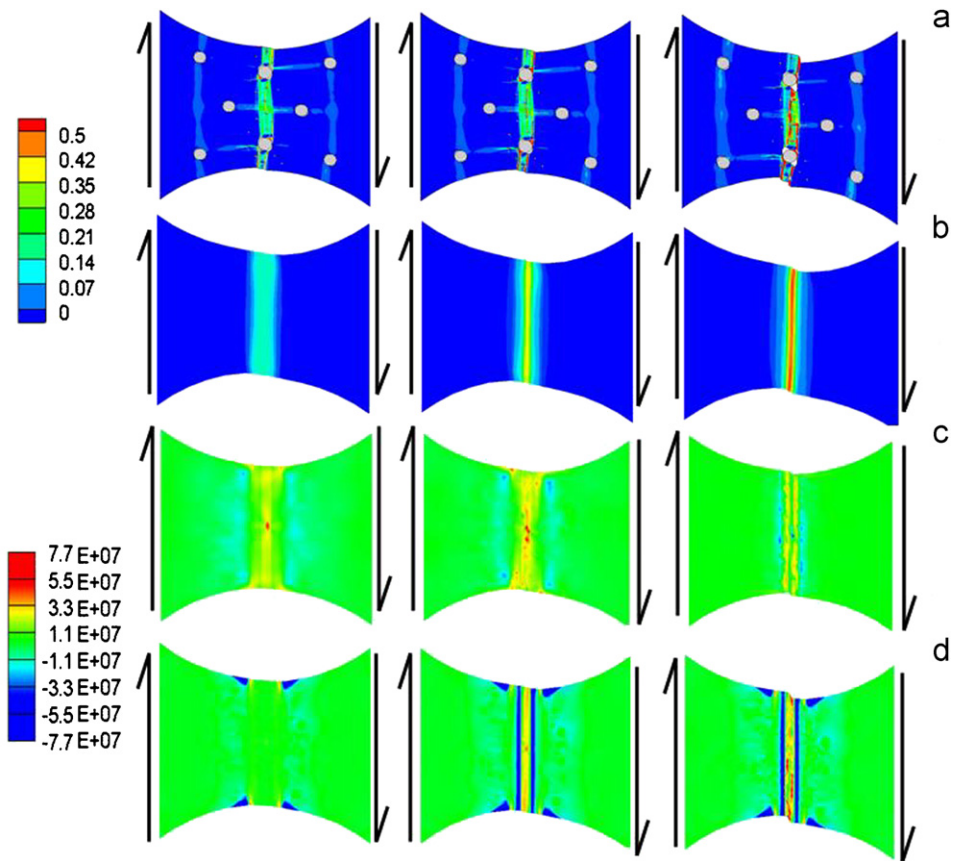


Fig. 12. (a) Snapshots of the plastic deformation of the shear specimen with explicit microstructure; (b–d) snapshots of the plastic deformation, micro- and submicro-stresses of the shear specimen using the three-scale material model.

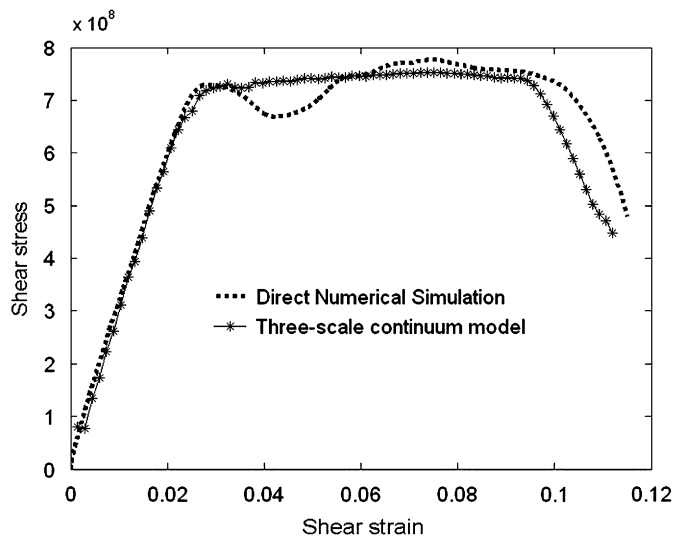


Fig. 13. Average shear stress–strain curve measured in the specimen.

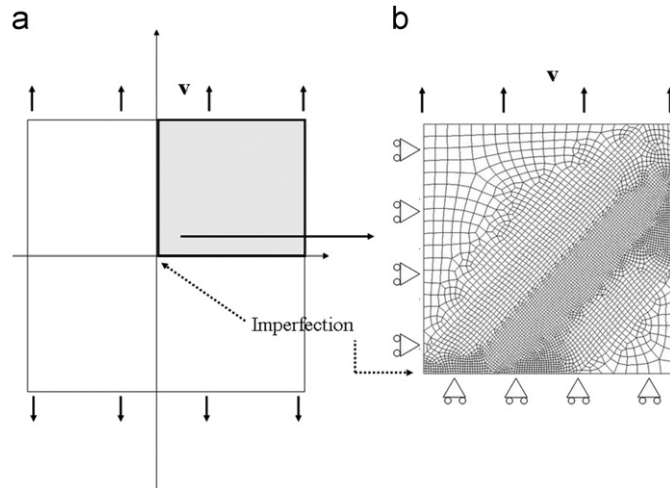


Fig. 14. Geometry, boundary conditions and finite element discretization of the tensile specimen.

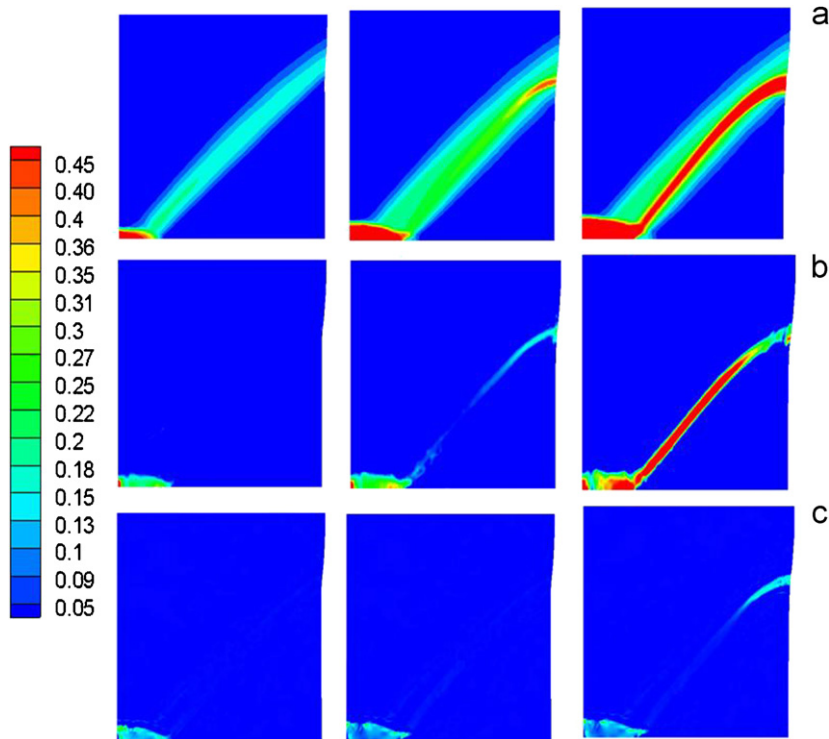


Fig. 15. Contours of effective plastic strain at the macro-, micro- and submicro-scales at different stages of deformation.

The evolution of effective plastic strains at macro-, micro- and submicro-scales are depicted in Fig. 15 for different times. Three stages of material failure are shown. The first stage corresponds to material instability at the bottom left corner of the specimen due to the imperfection. The interaction between the damaged zone and the free surface on the right creates a band of intense plastic strains at 45° promoting void nucleation from primary particles. The width of this shear band is related to the size  $\bar{\ell}^1$  associated with primary particles. As the central crack grows, the intensity of plastic strain in the shear band increases (with high triaxiality in the center and low triaxiality near the free boundary). Due to large shear strain levels near the free boundary, the

criterion for nucleation of secondary particles (Eq. (A.16)) occurs first in this area. Therefore, stage 2 can be observed near the boundary as the microscopic plastic strain  $E^1$  emerges (due to the micro-stress instability), starting from the free boundary and growing towards the crack. This inner shear band due to microvoid growth has a width that is related to the size  $\bar{\ell}^2$ . Stage 3, or the final stage is reached when microvoids coalesce. In the multi-scale model, microvoid coalescence (which is measured by the submicro-strain  $E^2$ ) can be observed to appear within the micro-shear band in the bottom right picture of Fig. 15. Although this simulation is realized under plane strain conditions, the resulting mode of failure can be compared with the “cup and cone” fracture of a cylindrical specimen in tension. Similarly to what is observed on fracture surfaces, the central region is due to nucleation, growth, and coalescence of voids from primary particles, due to the high level of triaxiality and the “shear lips” are related to microvoid nucleation around secondary particles, due to high level of shear in these regions.

## 5. Conclusions

In this study, the multi-scale theory of Vernerey et al. (2007) was successfully used to describe the multi-scale character of damage and failure in steel possessing particle distributions at two distinct scales. The proposed model has the following characteristics:

- The internal power is written in terms of the velocity, rate of deformation at the scale of primary particles and rate of deformation at the scale of secondary particles. This leads to a three-scale material model, whose governing equations consist of a set of three coupled differential equations.
- The constitutive relation in the plastic regime was written in terms of three yield functions characterizing degradation of the material at different scales.
- While the form of micro-scale yield function is purely phenomenological, most material constants are determined using a proper (statistical) averaging procedure.
- The model provides useful improvement compared to conventional models as it captures deformation history after onset of macroscopic instability.

The model was evaluated for both shear and tension. In shear, the solution provided by the three-scale micromorphic model was compared to the solution given by modeling explicit microstructures. We obtained good agreement between the two solutions, as the three-scale material was able to capture localizations occurring at two distinct length scales. The behavior in tension showed that the model was in-line with underlying mechanisms of fracture. It could predict failure from primary particle in the center of the notch and failure in a void sheet on the sides. This is similar to mechanisms observed in axisymmetric loading with the cup and cone fracture.

Many aspects still need to be explored and improved in the newly developed multi-scale continuum model. The first concerns determination of the constitutive relation. At micro-scales, the form of plastic potentials, evolution of plastic variables and so forth, were chosen empirically. A research direction could be to perform averaging operations simultaneously with macro-scale simulation, similarly to the global–local analysis introduced in Varvara Kouznetsova (2002) or the power equivalent approach proposed by Liu and McVeigh (Comp Mech 2007). From a computational perspective, two problems should be explored. One, when implementing the multi-scale model in the finite element method, the element size is required to be on the order of the smallest microstructural length scale. This can result in very expensive (time and cost) simulation on large domains. A solution to this problem resides in multi-scale numerical methods such as those developed in Wagner and Liu (2003), Wagner et al. (2004), Kadowaki and Liu (2004), McVeigh et al. (2006), and Liu et al. (2004, 2006, 1995). Finally, in modeling localization and failure of materials, it is of interest to model material deformation up to the point of failure. However, at this stage, the finite element methods yield inaccurate results before the final point of failure due to high element distortion. Numerical methods such as meshless methods may provide a solution to this problem (Li and Liu, 2002; Liu et al., 1995).

## Acknowledgments

The authors gratefully acknowledge the support of the ONR/DARPA D3D Digital Structure Consortium (award N00014-05-C-0241).

## Appendix A. Hierarchical modeling

### A.1. Homogenization at the scale of secondary particles

The yield function at the scale of secondary particles in Section 3.2 is written as

$$\Phi' = \left(\frac{\sigma'_{\text{eq}}}{\sigma_y}\right)^2 + 2q'_1 f' \cosh\left(\frac{3q'_2 \sigma'_m}{2\sigma_y}\right) - (1 + q'_3 (f')^2) = 0. \quad (\text{A.1})$$

The determination of the constants  $q'_1$ ,  $q'_2$  and  $q'_3$  in the yield function given in Eq. (13) is described in Appendix C.3. This yields the following set of constants:

$$q'_1 = 0.91, \quad q'_2 = 1.9, \quad q'_3 = 0.95. \quad (\text{A.2})$$

The evolution of accumulated plastic strain is obtained by invoking the equality of macroscopic and microscopic rates of plastic work:

$$\sigma' : D'^{\text{p}} = (1 - f') \sigma_y \dot{\epsilon}'_{\text{p}} \Rightarrow \dot{\epsilon}'_{\text{p}} = \frac{\sigma' : D'^{\text{p}}}{(1 - f') \sigma_y}, \quad (\text{A.3})$$

where  $\sigma_y$  is the yield stress of the matrix material. The evolution of the microvoid volume fraction  $f'$  is decomposed into three components. The first,  $f'_n$ , is due to the void nucleation from secondary particles, the second,  $f'_g$  is related to the growth of the void after nucleation has occurred, and finally, the third,  $f'_c$  represents the extra porosity arising from the coalescence process. We write

$$\dot{f}' = \dot{f}'_n + \dot{f}'_g + \dot{f}'_c. \quad (\text{A.4})$$

Due to the incompressibility of the matrix material, an increase of porosity is related to dilatational plastic strain rate  $\text{Tr}(\mathbf{D}'^{\text{p}})$  as follows:

$$\dot{f}'_g = (1 - f') \text{Tr}(\mathbf{D}'^{\text{p}}). \quad (\text{A.5})$$

Following Saje et al. (1982), the rate of microvoid nucleation is taken as

$$\dot{f}'_n = A'_1 \dot{\sigma}'_{\text{eq}} + \frac{B'_1}{3} \dot{\sigma}'_m, \quad (\text{A.6})$$

where the parameters  $A'_1$  and  $B'_1$  characterize the dependence of the nucleation rate on the equivalent stress rate and hydrostatic stress rate, respectively, and are functions of the stress and deformation history. Nucleation is assumed to follow a normal distribution around the mean value  $\epsilon'^{\text{sp}}_{\text{N}}$  of plastic strain as follows:

$$A'_1 = \frac{f'_{\text{N}}}{s' \sqrt{2\pi}} \exp\left(-\frac{1}{2} \left(\frac{\epsilon'_p - \epsilon'_{\text{N}}}{s' \sigma_y}\right)^2\right), \quad B'_1 = 0, \quad (\text{A.7})$$

where  $f'_{\text{N}}$  represents the volume fraction of secondary particle and  $s'$  is the standard deviation. Referring to Goods and Brown (1979) and based on a large amount of cell model simulation, the critical plastic strain depends on the amount of hydrostatic stress.

The nucleation model is investigated as a function of the decohesion energy at the interface of particle–matrix. Computationally, the bonds between the particle and the matrix material were modeled using non-linear cohesive elements. Following the previous study in McVeigh et al. (2007), the evolution of void coalescence can be written as follows:

$$\dot{f}'_c = B'_1 (1 - f') \text{Tr}(D'^{\text{p}}) + B'_2 \dot{\epsilon}'_{\text{p}}, \quad (\text{A.8})$$

where  $B'_1$  represents the acceleration of void growth in high triaxiality and  $B'_2$  was added to represent the shear driven void coalescence such that:

$$\begin{aligned} B'_1 &= 0, & B'_2 &= 0 & \text{before the onset of coalescence,} \\ B'_1 &> 0, & B'_2 &> 0 & \text{after the onset of coalescence.} \end{aligned} \quad (\text{A.9})$$

Cell modeling studies showed that the criterion for the onset of void coalescence can be expressed as follows:

$$f' + a_c \dot{\epsilon}'_p - b_c > 0, \quad (\text{A.10})$$

where  $a_c = 0.1222$  and  $b_c = -0.1236$ . In other words, coalescence takes place either at high void volume fraction or at high plastic strains. The trade-off between those quantities is given by the relation (A.10).

#### A.2. Homogenization at the scale of primary particles

The macroscopic yield function is written in the form:

$$\Phi = \left( \frac{\sigma_{\text{eq}}}{\sigma_y} \right)^2 - 1 + 2q_1(f^{\text{P}} + f^{\text{S}}) \cosh\left( \frac{3q_2\sigma_m}{2\sigma_y} \right) - q_3(f^{\text{P}} + f^{\text{S}})^2 = 0. \quad (\text{A.11})$$

The evolutions of void volume fraction nucleating from primary and secondary particles are taken in the following form:

$$\dot{f}^{\text{P}} = \dot{f}^{\text{n}} + \dot{f}^{\text{g}} \text{ and } \dot{f}^{\text{S}} = \dot{f}^{\text{c}}. \quad (\text{A.12})$$

The first term  $\dot{f}^{\text{n}}$  denotes the nucleation of voids around primary particles, the second  $\dot{f}^{\text{g}}$  represents the growth of those voids under the action of hydrostatic stress and finally,  $\dot{f}^{\text{c}}$  is the coalescence term. The coalescence stage can be explained with the void-sheet mechanism (Horstemeyer et al., 2000) as follows: as larger voids grow, the plastic strain in the matrix material increase significantly, leading to nucleation of the smaller population of voids. The newly nucleated microvoids are then free to grow and coalesce in the localization band often referred to as the void sheet. The rate of void nucleation from primary particles is written in the form used by Saje et al. (1982) as follows:

$$\dot{f}^{\text{n}} = A_1 \dot{\sigma}_{\text{eq}} + A_2 \dot{\sigma}_m. \quad (\text{A.13})$$

Void coalescence occurs by growth and coalescence of voids nucleating from secondary particles in a void sheet between larger cavities. Microscopic parameters such as secondary particle volume fractions, distribution or decohesion energy determine this mode of coalescence and are introduced to the macroscopic model via the material constants derived at the micro-scale. The form of the rate of void coalescence is assumed to depend on the rate of hydrostatic strain and plastic strain rate in the form:

$$\dot{f}^{\text{c}} = B(1 - f)\text{Tr}(D^{\text{P}}) + B_2 \dot{\epsilon}_p, \quad (\text{A.14})$$

where  $B$  represents the coalescence due to nucleation and growth of microvoids in high triaxiality and  $B_2$  represents the shear driven microvoid coalescence. Similar to the coalescence model at the micro-scale,  $B$  and  $B_2$  are such that:

$$\begin{aligned} B &= 0, & B_2 &= 0 & \text{before the onset of coalescence,} \\ B &> 0, & B_2 &> 0 & \text{after the onset of coalescence.} \end{aligned} \quad (\text{A.15})$$

The onset of void-sheet mechanism is related to the nucleation, growth and nucleation of small voids in between larger voids as the larger voids impose high plastic deformations in the surrounding regions. Hence, the criterion for void sheet driven coalescence is taken to be the void volume fraction of the larger voids  $f^{\text{P}}$ , and the equivalent plastic strain  $\epsilon_p$ . Based on the micromechanical response of the RVE, the onset of void sheet coalescence is identified by a sudden drop in the macroscopic stress. The average void volume fraction and plastic strain in the RVE are then monitored at this point for different states of triaxiality. This analysis is performed for different values of bonding energies at the secondary particles–matrix interface. Cell modeling shows that a linear function can be used to approximate the relationship between plastic strain and porosity at the onset of coalescence. In other words, the onset of void

sheet driven coalescence is on the straight line given by

$$f + a_{vs}\varepsilon_p - b_{vs}(\sigma^S) = 0, \quad (\text{A.16})$$

where  $a_{vs} = 0.0639$  and  $b_{vs}$  is a linear function of the debonding stress (in GPa):

$$b_{vs}(\hat{\sigma}^S) = (0.0043\hat{\sigma}^S + 0.0186). \quad (\text{A.17})$$

Eqs. (A.16) and (A.17) can be interpreted as follows. Void-sheet coalescence occurs either in high volume fraction and low plastic strain or in high plastic strain and low volume fraction. This can be explained by the fact that both an increase of volume fraction and plastic strain have a direct influence on the strains between larger voids. Finally, a stronger interface at the secondary particle/matrix, by postponing small void nucleation, has the effect of delaying the coalescence.

## Appendix B. Material models

### B.1. Material constants for Von-Mises model

The derivation of material constants of the generalized Von-Mises plasticity model is similar to the Drucker–Prager model presented in Section B.2 by setting  $\alpha = 0$ .

### B.2. Material constants for Drucker–Prager model

In this appendix, we show the derivation of material constants for the generalized Drucker–Prager model utilized for the constitutive relation at the microscale. Let us first develop an expression for the averaged deviatoric and volumetric stresses  $\bar{\boldsymbol{\beta}}^{1,\text{dev}}$ ,  $\bar{\bar{\boldsymbol{\beta}}}^{1,\text{dev}}$ ,  $\bar{\boldsymbol{\beta}}^{1,\text{m}}$  and  $\bar{\bar{\boldsymbol{\beta}}}^{1,\text{m}}$ . Following from Eq. (6), we can write:

$$\begin{aligned} \bar{\boldsymbol{\beta}}^{1,\text{dev}} &= \frac{1}{\bar{\Omega}^1} \int_{\bar{\Omega}^1} \boldsymbol{\beta}^{1,\text{dev}} \, d\Omega \quad \text{and} \quad \bar{\bar{\boldsymbol{\beta}}}^{1,\text{dev}} = \frac{1}{\bar{\Omega}^1} \int_{\bar{\Omega}^1} \boldsymbol{\beta}^{1,\text{dev}} \otimes \mathbf{y} \, d\Omega, \\ \bar{\boldsymbol{\beta}}^{1,\text{m}} &= \frac{1}{\bar{\Omega}^1} \int_{\bar{\Omega}^1} \beta^{1,\text{m}} \, d\Omega \quad \text{and} \quad \bar{\bar{\boldsymbol{\beta}}}^{1,\text{m}} = \frac{1}{\bar{\Omega}^1} \int_{\bar{\Omega}^1} \beta^{1,\text{m}} \mathbf{I} \otimes \mathbf{y} \, d\Omega. \end{aligned} \quad (\text{B.1})$$

Performing the above averaging operations, it is straightforward to show that the deviatoric and volumetric micro-stresses can be written as follows:

$$\begin{aligned} \bar{\beta}_{ij}^{1,\text{dev}} &= \bar{\beta}_{ij}^1 - \frac{1}{3} \bar{\beta}_{kk}^1 \delta_{ij} \quad \text{and} \quad \bar{\bar{\beta}}_{ijk}^{1,\text{dev}} = \bar{\beta}_{ijk}^1 - \frac{1}{3} \bar{\beta}_{llk}^1 \delta_{ij}, \\ \bar{\beta}^{1,\text{m}} &= \frac{1}{3} \bar{\beta}_{ii}^1 \quad \text{and} \quad \bar{\bar{\beta}}_i^{1,\text{m}} = \bar{\beta}_{kki}^1. \end{aligned} \quad (\text{B.2})$$

Next, the derivation of constants  $a^1$ ,  $b^1$  and  $c^1$  introduced in Eqs. (16) and (17) is addressed. We first introduce the rate of microscopic plastic strain  $\dot{\varepsilon}^1(\mathbf{x} + \mathbf{y})$  evaluated at a material point  $\mathbf{x} + \mathbf{y}$

$$\dot{\varepsilon}^1(\mathbf{x} + \mathbf{y}) = \sqrt{\frac{2}{3}(\mathbf{D}^{1,\text{p}}(\mathbf{x} + \mathbf{y}) - \mathbf{D}^{\text{p}}(\mathbf{x})) : (\mathbf{D}^{1,\text{p}}(\mathbf{x} + \mathbf{y}) - \mathbf{D}^{\text{p}}(\mathbf{x}))} \quad (\text{B.3})$$

and calculate an average of this quantity in the meso-domain  $\bar{\Omega}^1$

$$\dot{\bar{\varepsilon}}^1(\mathbf{x}) = \sqrt{\frac{1}{\bar{\Omega}^1} \int_{\bar{\Omega}^1} (\dot{\varepsilon}^1(\mathbf{x} + \mathbf{y}))^2 \, d\Omega}. \quad (\text{B.4})$$

Taking advantage of the fact that the rate of micro-deformation varies linearly in  $\bar{\Omega}^1$ , we obtain:

$$\dot{\bar{\varepsilon}}^1 = \sqrt{\frac{2}{3}(\mathbf{D}^{1,\text{p}} - \mathbf{D}^{\text{p}}) : (\mathbf{D}^{1,\text{p}} - \mathbf{D}^{\text{p}}) + c^1 \bar{\varepsilon}^1 \mathbf{D}^{1,\text{p}} \vec{\nabla} : \mathbf{D}^{1,\text{p}} \vec{\nabla}}, \quad (\text{B.5})$$

where the constant  $c^1 = 1/18$ . Extending the idea of de Borst (1993) for the Druker–Prager model, the material constants  $a^1$  and  $b^1$  are now determined based on the equality of the plastic multiplier and the equivalent plastic strain:

$$\dot{E}^1 = \dot{\lambda}^1 \sqrt{1 + 2\alpha^2}. \tag{B.6}$$

Let us first write the plastic flow directions  $\bar{\mathbf{r}}^1$  and  $\bar{\bar{\mathbf{r}}}^1$  as follows:

$$\begin{aligned} \bar{\mathbf{r}}^1_{ij} &= \frac{\partial \Phi^1}{\partial \bar{\beta}^1_{ij,dev}} = \frac{3}{2} \frac{\bar{\beta}^1_{ij,dev}}{B_{eq}^1} + \alpha \frac{\beta^{1,m}}{B_m} \delta_{ij}, \\ \bar{\bar{\mathbf{r}}}^1_{ijk} &= \frac{\partial \Phi^1}{\partial \bar{\beta}^1_{ijk}} = \left(\frac{a^1}{\bar{\ell}^1}\right)^2 \frac{\bar{\beta}^1_{ijk,dev}}{B_{eq}^1} + \alpha \left(\frac{a^1}{\bar{\ell}^1}\right)^2 \frac{\bar{\beta}^1_{k,m}}{B_m} \delta_{ij}. \end{aligned} \tag{B.7}$$

Let us now write the rate of plastic strain in terms of the plastic directions  $\bar{\mathbf{r}}^1$  and  $\bar{\bar{\mathbf{r}}}^1$ :

$$(\mathbf{D}^{1,p} - \mathbf{D}^p) = \dot{\lambda}^1 \bar{\mathbf{r}}^1 \text{ and } \mathbf{D}^{1,p} \vec{\nabla} = \dot{\lambda}^1 \bar{\bar{\mathbf{r}}}^1. \tag{B.8}$$

Using the above relations in Eq. (B.5), we obtain

$$\dot{E}^1 = \dot{\lambda}^1 \sqrt{\frac{2}{3} \bar{\mathbf{r}}^1 : \bar{\mathbf{r}}^1 + (c^1 \bar{\ell}^1)^2 \bar{\bar{\mathbf{r}}}^1 : \bar{\bar{\mathbf{r}}}^1}. \tag{B.9}$$

We can develop the above expression by using the expression of the plastic directions given in Eq. (B.7) to obtain

$$\begin{aligned} (\dot{E}^1)^2 &= (\dot{\lambda}^1)^2 \frac{(3/2) \bar{\beta}^1_{ij,dev} : \bar{\beta}^1_{ij,dev} + (c^1 \bar{\ell}^1)^2 (a^1/\bar{\ell}^1)^4 \bar{\beta}^1_{ijk,dev} : \bar{\beta}^1_{ijk,dev}}{B_{eq}^1} \\ &\quad + (\dot{\lambda}^1)^2 3\alpha^2 \frac{(2/3) \bar{\beta}^1_{k,m} \bar{\beta}^1_{k,m} + (c^1 \bar{\ell}^1)^2 (b^1/\bar{\ell}^1)^4 \bar{\beta}^1_{k,m} \cdot \bar{\beta}^1_{k,m}}{B_m^1}. \end{aligned} \tag{B.10}$$

Using Eqs. (B.5) and (B.10), we can determine the material constants  $a^1$  and  $b^1$  as a function of  $c^1$ . It is straightforward to show that in this case, we must have

$$a^1 = \frac{1}{c^1} = 18 \quad \text{and} \quad b^1 = \sqrt{\frac{2}{3}} \frac{1}{c^1} = 18 \sqrt{\frac{2}{3}}. \tag{B.11}$$

### Appendix C. Cell model

#### C.1. Periodic boundary conditions

Referring to Fig. 16, consider the initially rectangular periodic RVE of width  $D_1$ , height  $D_2$  whose directions are aligned with the axes  $y_i$ . Let us choose four nodes, each belonging to a different boundary and write their displacement as follows:

- $u_1^L$  and  $u_2^L$  are the displacements of the nodes on the left boundary in the  $y_1$  and  $y_2$  directions, respectively.
- $u_1^R$  and  $u_2^R$  are the displacements of the nodes on the right boundary in the  $y_1$  and  $y_2$  directions, respectively.

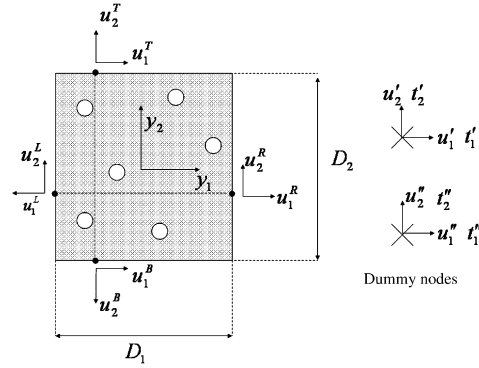


Fig. 16. Set up of the cell model for periodic boundary conditions.

- $u_1^T$  and  $u_2^T$  are the displacements of the nodes on the top boundary in the  $y_1$  and  $y_2$  directions, respectively.
- $u_1^B$  and  $u_2^B$  are the displacements of the nodes on the bottom boundary in the  $y_1$  and  $y_2$  directions, respectively.

In order to apply the periodic boundary conditions, let us introduce two dummy nodes  $N'$  and  $N''$  of respective displacements  $u'$  and  $u''$ . The displacements of nodes on the boundaries of the RVE are then constrained as follows:

$$\begin{aligned}
 u_1^R - u_1^L &= u'_1, \\
 u_2^T - u_2^B &= u'_2, \\
 u_1^T - u_1^B &= u''_1, \\
 u_2^R - u_2^L &= u''_2.
 \end{aligned}
 \tag{C.1}$$

This can be done in the commercial software ABAQUS<sup>®</sup> by using the linear constraint option. With those constraints, only the four boundary conditions on the dummy node need to be prescribed and the average true strain in the RVE is then given by the following relation:

$$\begin{bmatrix} \varepsilon_{11} & \varepsilon_{12} \\ \varepsilon_{21} & \varepsilon_{22} \end{bmatrix} = \begin{bmatrix} \log\left(1 + \frac{u'_1}{D_1}\right) & \log\left(1 + \frac{u''_1}{D_2}\right) \\ \log\left(1 + \frac{u'_2}{D_2}\right) & \log\left(1 + \frac{u''_2}{D_1}\right) \end{bmatrix}.
 \tag{C.2}$$

Moreover, the linear constraint implies that the total reaction forces on the boundaries of the RVE are the forces  $f'$  and  $f''$  on the dummy nodes. The average Cauchy stress in the RVE defined as the boundary traction per unit area is therefore written as follows:

$$\begin{bmatrix} \sigma_{11} & \sigma_{12} \\ \sigma_{21} & \sigma_{22} \end{bmatrix} = \begin{bmatrix} \frac{t'_1}{D_2 + u'_2} & \frac{t''_1}{D_1 + u'_1} \\ \frac{t''_2}{D_2 + u'_2} & \frac{t'_2}{D_1 + u'_1} \end{bmatrix}.
 \tag{C.3}$$

C.2. Constant stress ratio with periodic BC

In this section, we describe the technique to keep the stress ratio  $R = \sigma_{11}/\sigma_{22}$  constant through the simulation. This technique is based on the work of Socrate (1995) and is done by prescribing the average strain  $\varepsilon_{22}$  through the displacement  $u'_2$  and applying a pressure  $p = \sigma_{11}$  on the right and left boundaries of the RVE.

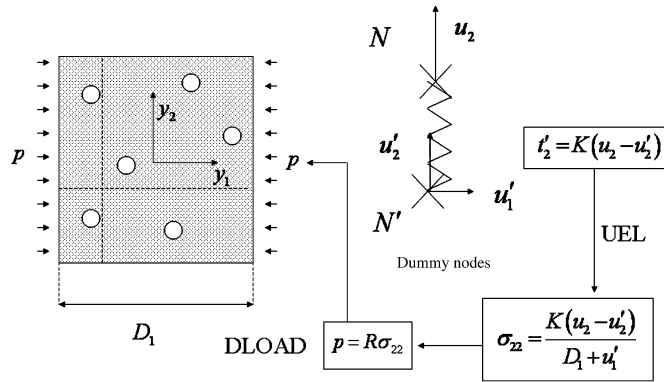


Fig. 17. Set up of the cell model for boundary conditions with constant stress ratio.

This is done via the definition of a user-element in ABAQUS<sup>®</sup> (subroutine UEL) and the subroutine DLOAD.

The procedure consists of computing the average stress  $\sigma_{22}$  during the simulation and applying the pressure  $p$  on the sides such that we have:

$$p = R\sigma_{22}. \tag{C.4}$$

However, as the RVE is displacement controlled, the stress  $\sigma_{22}$  is not explicitly known during the simulation and must be determined through a special procedure. The latter consists in defining a user element subroutine that computes the stress  $\sigma_{22}$  at each time step and pass it to the subroutine DLOAD that applies the resulting pressure  $p$  on the left and right boundaries.

Referring to Fig. 17, we first introduce an additional dummy node  $N$ , located straight above node  $N'$  such that the user element consists of two nodes and three degree of freedom as follows:

- the displacement  $u_2$  of node  $N$ ;
- the displacements  $u'_1$  and  $u'_2$  of node  $N'$ .

The procedure consists of applying the vertical displacement boundary condition on node  $N$  instead of  $N'$  and linking the two nodes with a stiff spring of stiffness  $K$ . The tensile force  $t'_2$  on node  $N'$  is therefore given by

$$t'_2 = K(u_2 - u'_2). \tag{C.5}$$

It is then straightforward to obtain the stress  $\sigma_{22}$  with the knowledge of  $u'_1$ ,

$$\sigma_{22} = \frac{t'_2}{D_1 + u'_1} = \frac{K(u_2 - u'_2)}{D_1 + u'_1}. \tag{C.6}$$

This value can then be transferred to the subroutine DLOAD so that the pressure is given by Eq. (C.4).

### C.3. Method to fit the yield function

In what follows, we describe the micromechanical cell simulation of the representative volume element used to find the material constants introduced in Section 3. The computational results serve two purposes: first, they are used to fit the material constants that appear in the macroscopic yield function and second, they serve in the determination of the constants in the evolution of the void volume fraction. The simulation are performed on a two-dimensional square domain randomly filled with voids of volume fraction is  $f_0$ . Furthermore, we assume that the material is made of a periodic arrangement of such volumes, so that the boundary conditions can be described by the periodic boundary conditions introduced in Appendix C.1. During deformation, the principal strains are aligned with the axes of the initial cell so that the average shear strains  $\epsilon_{12}$  and  $\epsilon_{21}$  vanish

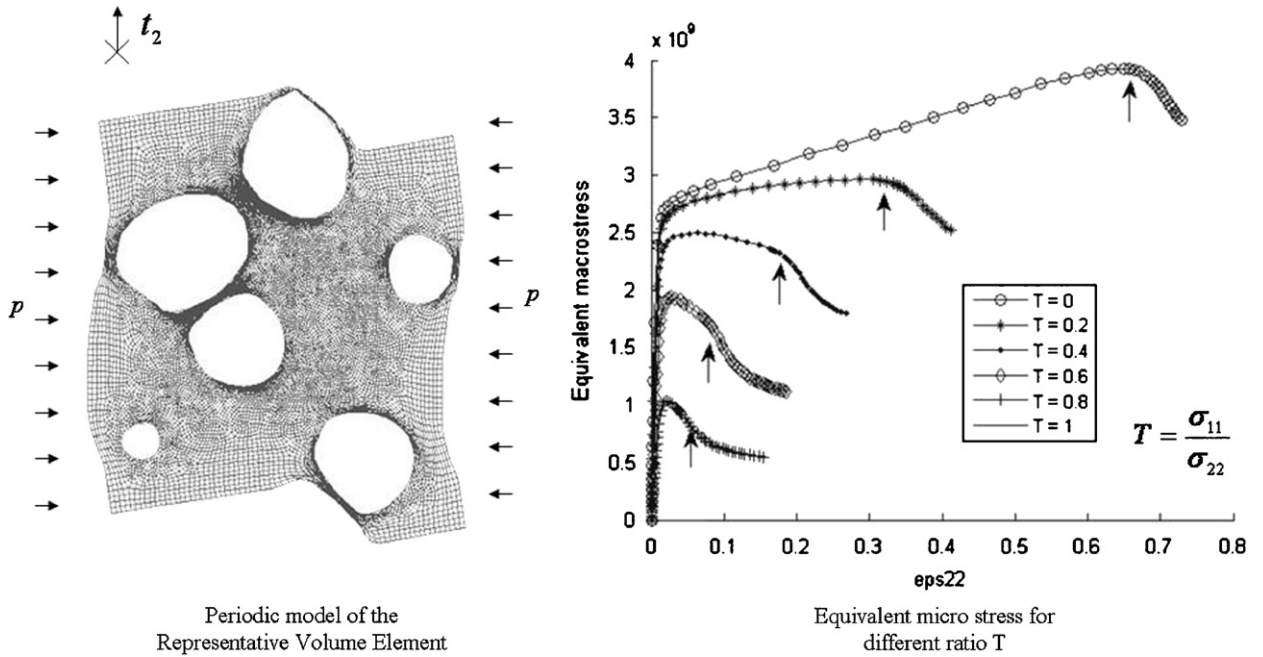


Fig. 18. RVE for porous material subject to periodic boundary conditions and associated tensile stress–strain curves for various triaxialities.

at all time. Finally, the average strains  $\varepsilon_{11}$  and  $\varepsilon_{22}$  are such that the ratio  $R = \sigma_{11}/\sigma_{22}$  of principal stresses is constant throughout the simulation. It is done by using the user element option in commercial finite element software ABAQUS<sup>®</sup> as described in Appendix C.2.

The averaged stress on the RVE is given by Eq. (12). Using the divergence theorem, we can write the average Cauchy stress in terms of the surface traction forces  $\tilde{t}$ :

$$\boldsymbol{\sigma} = \frac{1}{\Omega} \int_{\tilde{f}} \tilde{t} \otimes \mathbf{y} \, d\Omega. \quad (\text{C.7})$$

The equivalent stress  $\sigma_{\text{eq}}$  and mean stress  $\sigma_{\text{m}}$  can be written in terms of the stress  $\sigma_{22}$  as follows:

$$\begin{aligned} \sigma_{\text{m}} &= \frac{1}{2}(\sigma_{11} + \sigma_{22}) = \frac{R+1}{2}\sigma_{22}, \\ \sigma_{\text{eq}} &= \frac{\sqrt{3}}{2} \sqrt{(\sigma_{22} - \sigma_{11})^2} = \frac{\sqrt{3}}{2}(1-R)|\sigma_{22}|, \quad R \leq 1. \end{aligned} \quad (\text{C.8})$$

We also introduce the triaxiality  $T$  as the ratio of the hydrostatic stress and the equivalent stress. In the simulation, the stress  $\sigma_{22}$  remains positive and we can write:

$$T = \frac{\sigma_{\text{m}}}{\sigma_{\text{eq}}} = \frac{1}{\sqrt{3}} \frac{R+1}{1-R}. \quad (\text{C.9})$$

It is then possible to rewrite the yield function introduced in Eq. (16) in terms of the triaxiality parameter as follows:

$$\Phi(X, f) = X^2 + 2q_1 f \cosh\left(\frac{3q_3}{2} TX\right) - (1 + (q_2)^2) = 0. \quad (\text{C.10})$$

where  $X = \sigma_{\text{eq}}/\sigma_y$ . Thus, for each simulation for a constant value of  $T$ , we obtain a curve  $X(f)$  as shown in Fig. 18. This can be used for the calibration of material constants in  $\Phi(X, f)$  using the least-square method.

## References

- Bazant, Z., Jirasek, M., 2002. Nonlocal integral formulations of plasticity and damage: survey of progress. *J. Eng. Mech.* 128, 1119–1149.
- Cowie, J.G., Azrin, M., Olson, G.B., 1989. Microvoid formation during shear deformation of ultrahigh strength steels. *Metall. Trans.* 20A, 143–153.
- de Borst, R., 1993. A generalization of j2-flow theory for polar continua. *Comput. Methods Appl. Mech. Eng.* 103, 347–362.
- Freeman, A.J., 2002. Materials by design and the exciting role of quantum computation/simulation. *J. Comput. Appl. Math.* 149, 27–56.
- Geng, W.T., Freeman, A.J., Olson, G.B., 2001. Influence of alloying additions on grain boundary cohesion of transition metals: first-principles determination and its phenomenological extension. *Phys. Rev. B* 63, 165415, 1–9.
- Gologanu, M., Leblond, J.B., Perrin, G., Devaux, J., 1995. *Continuum Micromechanics*. Springer, Berlin, p. 61.
- Goods, S.H., Brown, L.M., 1979. Nucleation of cavities by plastic deformation. *Acta Metall.* 27, 1–15.
- Gurson, A.L., 1977. Continuum theory of ductile rupture by void nucleation and growth: Part I; yield criteria and flow rules for porous ductile media. *ASME J. Eng. Mater. Technol.* 99, 2–15.
- Hao, S., Liu, W.K., Moran, B., Vernerey, F., Olson, G.B., 2004. Multiple-scale constitutive model and computational framework for the design of ultra-high strength, high toughness steels. *Comput. Methods Appl. Mech. Eng.*
- Horstemeyer, M.F., Lathrop, J., Gokhale, A.M., Dighe, M., 2000. Modeling stress state dependent damage evolution in a cast Al–Si–Mg aluminum alloy. *Theor. Appl. Frac. Mech.* 33, 31–47.
- Kadowaki, H., Liu, W.K., 2004. Bridging multi-scale method for localization problems. *Comput. Methods Appl. Mech. Eng.* 193, 3267–3302.
- Leblond, J.B., Perrin, G., Devaux, J., 1994. Bifurcation effects in ductile metals with damage delocalization. *ASME J. Appl. Mech.* 61, 236–242.
- Lee, K., Ghosh, S., 1999. A microstructure based numerical method for constitutive modeling of composite and porous materials. *Mater. Sci. Eng. A* 272, 120–133.
- Li, S., Liu, W.K., 2002. Meshfree and particle methods and their applications. *Appl. Mech. Rev.* 55, 1–34.
- Liu, W.K., Jun, S., Zhang, Y.F., 1995. Reproducing kernel particle methods. *Int. J. Numer. Methods Fluids* 20, 1081–1106.
- Liu, W.K., Karpov, E.G., Zhang, S., Park, H.S., 2004. An introduction to computational nano mechanics and materials. *Comput. Method Appl. Mech. Eng.* 193 (17–20), 1529–1578.
- Liu, W.K., Karpov, E., Park, H.S., 2006. *Nano Mechanics and Materials: Theory, Multiscale Methods, and Applications*. Wiley, New York.
- McVeigh, C., Vernerey, F.J., Liu, W.K., Brinson, C., 2006. Multiresolution analysis for material design. *Comput. Methods Appl. Mech. Eng.* 195 (37–40), 5053–5076.
- McVeigh, C., Vernerey, F., Liu, W.K., Moran, B., Olson, G., 2007. An interactive microvoid shear localization mechanism in high strength steels. *J. Mech. Phys. Solids* 55 (2), 225–244.
- Needleman, A., Tvergaard, V., 1984. An analysis of ductile rupture in notched bars. *J. Mech. Phys. Solids* 32, 461–490.
- Nemat-Nasser, S., Hori, M., 1999. *Micromechanics: Overall Properties of Heterogeneous Materials*. North-Holland, Amsterdam.
- Pardoën, T., Hutchinson, J.W., 2000. An extended model for void growth and coalescence. *J. Mech. Phys. Solids* 48, 2467–2512.
- Perrin, G., Leblond, J., 2000. Accelerated void growth in porous ductile solids containing two populations of cavities. *Int. J. Plasticity* 16, 91–120.
- Pijaudier-Cabot, G., Bazant, Z., 1987. Nonlocal damage theory. *J. Eng. Mech.* 113 (10, Oct), 1512–1533.
- Rice, J.R., Tracey, D.M., 1969. On the ductile enlargement of voids in triaxial stress fields. *J. Mech. Phys. Solids* 17, 201–217.
- Saje, M., Pan, J., Needleman, A., 1982. Void nucleation effects on shear localization in porous plastic solids. *Int. J. Fract.* 19, 163–182.
- Socrate, S., 1995. *Mechanics of microvoid nucleation and growth in high-strength metastable austenitic steels*. Ph.D. Thesis.
- Tvergaard, V., 1982. Ductile fracture by cavity nucleation between larger voids. *J. Mech. Phys. Solids* 30, 265–286.
- Tvergaard, V., 1988. 3d-analysis of localization failure in a ductile material containing two size-scales of spherical particles. *Eng. Fract. Mech.* 31, 421–436.
- Tvergaard, V., Needleman, A., 1995. Nonlocal effects in ductile fracture by cavitation between larger voids. *Comput. Plasticity Fund. Appl.*, 963–973.
- Tvergaard, V., Needleman, A., 1997. Nonlocal effects on localization in a void-sheet. *Int. J. Solids Struct.* 34, 2221–2238.
- Varvara Kouznetsova, 2002. *Computational homogenization for the multi-scale analysis of multi-phase materials*. Ph.D. Thesis, Technische Universiteit Eindhoven.
- Vernerey, F.J., McVeigh, C., Liu, W.K., Moran, B., Tewari, D., Parks, D., Olson, G., 2006. 3D computational modeling of shear dominated ductile failure of steel. *J. Miner. Met. Mater. Soc.*, 45–51.
- Vernerey, F.J., Liu, W.K., Moran, B., 2007. Multi-scale micromorphic theory for hierarchical materials. *J. Mech. Phys. Solids*, doi:10.1016/j.jmps.2007.04.008.
- Wagner, G.J., Liu, W.K., 2003. Coupling of atomistic and continuum simulations using a bridging scale decomposition. *J. Comput. Phys.* 190, 249–274.
- Wagner, G., Karpov, E.G., Liu, W.K., 2004. Molecular dynamics boundary conditions for regular crystal lattices. *Comput. Method Appl. Mech. Eng.* 193, 1579–1601.